Analogue modeling of large-transport thrust faults in evaporites-floored basins: Example of the Chazuta Thrust in the Huallaga Basin, Peru

Sandra Borderie, Bruno Vendeville, Fabien Graveleau, César Witt, Pierre Dubois, Patrice Baby, Ysabel Calderon

Analogue modeling of large-transport thrust faults in evaporites-floored basins: example of the Chazuta Thrust in the Huallaga Basin, Peru.

Sandra BORDERIE[a,1,*], Bruno C. VENDEVILLE[a], Fabien GRAVELEAU[a], César WITT[a], Pierre DUBOIS[a,2], Patrice BABY[b], and Ysabel CALDERON[c]

[*] Corresponding author: University of Fribourg, Department of Geosciences, Chemin du Musée 6, 1700 Fribourg, Switzerland - sandra.borderie@unifr.ch - 0041 26 300 89 34

[a] Univ. Lille, CNRS, Univ. Littoral Côte d'Opale, UMR CNRS 8187, LOG, Laboratoire d'Océanologie et de Géosciences, F 59 000 Lille, France. bruno.vendeville@univ-lille.fr fabien.graveleau@univ-lille.fr cesar.witt@univ-lille.fr duboispierre11@gmail.com

[b] Géosciences Environnement Toulouse (GET), Université de Toulouse, CNRS UMR 5563 / UR 234 IRD / UPS Toulouse / CNES, 14 Avenue Edouard Belin, 31400 Toulouse, France. patrice.baby@ird.fr

[c] PERUPETRO S.A., Avenida Luis Aldana n°320, San Borja, Lima 41, Peru. ycalderon@perupetro.com.pe

Keywords

Huallaga Basin; Chazuta Thrust; evaporitic *décollement*; analogue modeling; strain localization; surface processes

[1] Present address: University of Fribourg, Department of Geosciences, Chemin du Musée 6, 1700 Fribourg, Switzerland.

[2]Present address: Perenco – Oil and Gas, 8 Hanover Square, London W1S 1HQ, England.

Abstract

The Huallaga Basin is a deformed foreland basin located in North Peru. The basin comprises several syntectonic depocenters. The most significant is the Biabo Syncline located at the back of the Chazuta Thrust, a long, flat-floored thrust detaching on an evaporitic *décollement*, which has accommodated more than 40 km of horizontal displacement. The hangingwall of the Chazuta Thrust has remained remarkably intact with little or no internal deformation and has incorporated a large volume of evaporites at its base.

In order to unravel the formation and evolution of this thrust, we conducted a series of physical experiments that tested the role of various parameters. The goal is to investigate a system in which most of the deformation is accommodated in the frontal part of the chain (Chazuta Thrust), whereas deformation of the thrust sheet itself remains minor.

Results from our experimental investigations suggest that the three key parameters that have allowed for such a long-lived, large-slip frontal thrust to operate are (1) the wedge-shaped syn-kinematic sedimentation, (2) the presence of the Biabo Syncline, which acted as a bulldozer pushing the evaporites forward, forcing their distal inflation and (3) the erosion at the front that favored farther advance of the frontal thrust, dragging passively large volumes of evaporites along with it.

1 Introduction

It has long been demonstrated that the dynamics of fold-and-thrust belts (FTBs) is notably controlled by the interaction between tectonic and climate surface processes (erosion and sedimentation) (e.g. Dahlen, 1990; Whipple, 2009; Willett et al., 1993). However, getting

direct field evidence proving this has been challenging. Analogue and numerical modeling has greatly helped in better understanding the mechanisms by which both erosion and sedimentation can modify the mechanical equilibrium of such accretionary systems (see reviews by Buiter, 2012; Graveleau et al., 2012). Primarily, syntectonic sedimentation exerts a first-order control on the number and spacing of thrusts, with deposition of thicker, wedge-shaped sediments favoring the formation of longer, somewhat "rigid" thrust sheets (*e.g.* Bonnet et al., 2008; Fillon et al., 2013; Mugnier et al., 1997; Wu and McClay, 2011). By reducing the average slope of the wedge, sedimentation reduces thrust advance in the outer parts of the belt. In order to maintain the critical wedge, older structures have to be reactivated at the hinterland (Huiqi et al., 1992; Boyer, 1995; Storti and McClay, 1995; Simpson, 2006; Stockmal et al., 2007; Wu and McClay, 2011). Similarly, erosion prevents deformation from propagating toward the foreland and therefore reduces the length of the belts. It reduces the number of active thrusts and therefore increases their lifetime (Koyi et al., 2000; McClay and Whitehouse, 2004; Cruz et al., 2010).

The term overthrust faulting was first used by Hubbert and Rubey (1959) on the basis of a former definition by Billings (1954) to describe flat, spectacular allochthonous geological features along which large masses of rock have been displaced along great distances. Large transport thrust faults (i.e. displacement greater than 10 km) have been reviewed using displacement-scale relationships (*e.g*. Bergen and Shaw, 2010; Kim and Sanderson, 2005). Some examples exist along the McConnell thrust in the Canadian Rockies (Elliott, 1976), the Glencoul thrust in the Moine thrust belt of Scotland (Coward et al., 1980), the Midi Thrust in the Ardennes massif of the Northern Europe Variscan belt (Lacquement et al., 1999), the Salt Range in Pakistan (Grelaud et al., 2002) and the Hotian Thrust in the Tarim Basin

(Wang et al., 2014), among others. However, the mechanisms by which such long-transport thrusts form have been poorly addressed in the past by neither numerical nor analogue modeling techniques; although much progress has been made in determining the magnitude of fault and crustal strength (Suppe, 2007, 2014).

The main issue in reproducing long-transport thrust using analogue modeling is the great difficulty of accommodating most (if not all) the shortening along one single structure. In this work, we present a set of analogue models, where parameters such as syntectonic sedimentation, basal detachment tilting, pre-kinematic tabular sedimentary cover and erosion of the frontal structures have been tested, leading to different evolutionary scenarios. Our analogue modeling protocol is inspired from the current knowledge of the structural and sedimentary architecture of the Huallaga Basin in north Peru (Figure 1). This basin is part of the modern Andean retro-foreland basin system in which compressional structures are largely influenced by the presence of evaporites. For instance, the major Chazuta Thrust accommodates at least 40 km of horizontal transport (i.e. ~50% of shortening of the FTB, (Hermoza et al., 2005; Calderon et al., 2017a, 2017b), with very little strain within the allochthonous thrust sheet and a large volume of evaporites incorporated into the hangingwall.

2 Geodynamic setting and structure of the Huallaga Basin

The Andean FTB extends across more than 5000 km, from Colombia and Venezuela in the North, to Patagonia and the Tierra del Fuego in the South. This is one of the most well-developed retro-arc, non-collisional FTB worldwide. Very diverse tectonic settings have

86 occurred since the Paleozoic to the Present Day from compressional, extensional and
87 strike-slip (e.g. Macellari and Hermoza, 2009; Ramos, 2010).

88 The Sub-Andean segment of Peru is part of the deformed retro-foreland basin system of the
89 Andes and corresponds to one of the most segmented sections of the Andean FTB (Figure
90 1). It can be divided into four main deformed foreland basins having different geological
91 configurations. From North to South these include the Santiago, Huallaga, Ucayali-Camisea
92 and Madre de Dios Basins and related fold-and-thrust belts (Figure 1). From the Huallaga
93 Basin to the Madre de Dios Basin the parameters controlling the style and amount of
94 deformation, as well as the width of the FTB, change drastically (e.g. McGroder et al., 2015).
95 Along-strike variations in FTB architecture have been ascribed to differences in basement
96 composition, lithosphere rigidity, climate variations, ridge subduction, distance from the
97 tectonic driving force, varying stress orientations relative to crustal fabrics, plate
98 subduction regime, and differences in pre-deformational settings (e.g. Espurt et al., 2008;
99 Gil Rodriguez et al., 2001; Kley et al., 1999; Macellari and Hermoza, 2009; McQuarrie et al.,
100 2008; Ramos, 2010; Ramos and Folguera, 2009).

101 The Huallaga Basin corresponds to a wedge-top basin (Hermoza et al., 2005) according to
102 the foreland model subdivision of DeCelles and Giles (1996). It is bounded to the West by
103 the Eastern Cordillera and to the East by the Marañon basin. Its northern and southern
104 limits are the Santiago Basin and the Ucayali Basin, respectively (Figures 1 and 2). Several
105 balanced and restored cross sections in the central part of the basin show that deformation
106 is the result of interaction between thin- and thick-skinned processes (Gil Rodriguez, 2001;
107 Hermoza et al., 2005; Eude et al., 2015; Calderon et al., 2017b). Thin-skinned deformation
108 is largely controlled by the presence of thick evaporitic series. Nevertheless, because of the

few constraints obtained by seismic and well data, different models have been proposed to explain the contractional deformation of the Huallaga Basin. They include inversion of Permo-Triassic grabens (*e.g*. Hermoza et al., 2005) and reactivation of Permian, basement-related thrusts verging towards the hinterland (Eude et al., 2015; Calderon et al., 2017a, 2017b). In their structural interpretation (Figure 3), Calderon et al. (2017b) infer there was a reactivation of west-verging basement thrusts inherited from a Permian fold-and-thrust belt under the Huallaga Basin. These authors also reinterpreted the chronostratigraphy of the area, suggesting that evaporites of the Huallaga Basin are late Permian in age and belong to the Shinai Formation (Figure 3). Thermochronological data and sequential restoration indicate that deformation began between 30 and 24 Ma to the East of the Eastern Cordillera by the reactivation of the basement faults and the formation of thrusts that root into the evaporitic *décollement* (Eude et al., 2015). This is in agreement with the work of Hermoza et al. (2005), which states that a foredeep depozone was present in the Huallaga basin at that time.

In map view, the basin geometry has an arcuate shape (Figure 2). In the central part of the basin, the structures are parallel to each other and strike orthogonally with respect to the direction of shortening. In contrast, in the northern and southern parts of the basin, the structures are oblique with respect to the shortening direction. This basin has a detachment-related salient geometry controlled by the presence of an evaporitic *décollement* that acts as a regional detachment and modifies the along-strike contractional structures (Macedo and Marshak, 1999).

We used three seismic sections to interpret and illustrate the geometry of the Huallaga Basin. Their location is indicated on the morphostructural map in Figure 2. The basin

shows a vertically and horizontally compartmentalized structuration. The shallow part of the basin is characterized by the Chazuta Thrust that corresponds to a fault-bend fold rooting at depth into the late Permian evaporitic *décollement*, and accommodates a large horizontal displacement (at least 40 km, Figures 2, 3 and 4). In the eastern part of the basin, major thrust systems (*e.g.* Chazuta and Shanusi Thrusts) mark the deformation front. The upper-frontal part of these thrusts has been eroded, and Cretaceous rocks crop out there. Erosion is marked by truncated reflectors on the seismic profiles (Figures 4 and 5). The western part of the basin is characterized by the Biabo Syncline, presently located on the hangingwall of the major Chazuta Thrust (Figures 3 to 6). The Biabo Syncline comprises a 6-7 km thick pile of Eocene-Pliocene syn-tectonic sediments (Hermoza et al., 2005). The Biabo Anticline is a fault-propagation fold that offsets the Neogene series (Figures 3 and 6). Apatite fission-track analyses along the Chazuta system yielded cooling ages of approximately 16 Ma, which are interpreted to be caused by thrust-related uplift (Eude et al., 2015).

The Chazuta thrust sheet is almost non-deformed in the center of the basin (Figures 2, 3 and 4) but its northern and southern parts shows a series of thrusts and backthrusts that deformed the hangingwall, although only minor slip is accommodated along each fault (Figures 2, 5 and 6). Another feature well illustrated on the seismic profiles is that a large volume of evaporites moved up along with the thrust sheet, remaining part of the hangingwall. These evaporites are therefore placed in an allochthonous position (Figures 3, 4 and 5), a feature rarely seen in contractional evaporites-related FTB (Costa and Vendeville, 2002), but common in salt tongues in the US Gulf of Mexico (Amery, 1969;

154 Worrall and Snelson, 1989; Wu et al., 1990b, 1990a; Nelson, 1991; Peel et al., 1995; Rowan,
155 1995).

156 The top of the Chazuta Thrust footwall is clearly imaged only on a couple of seismic
157 sections (Figures 4 and 5) and was not reached by the only well drilled in the area
158 (Posanillo Well: Figure 6, see location in Figure 2). In the footwall of the Chazuta Thrust,
159 the *décollement* is thinner than in the hangingwall. It has an autochthonous position and
160 created a series of salt pillows (Figures 4 and 5). There are doubts about the processes
161 controlling deformation in the footwall because seismic imaging beneath the evaporites is
162 poor. Most of footwall geometry constraints are indirectly inferred from restoration and
163 balanced cross sections. In the sequential restoration by Calderon et al. (2017b, 2017a), the
164 Biabo Anticline and the west-verging basement thrusts were poorly developed at the time
165 of middle Eocene. Then, thin- and thick-skinned deformation propagated simultaneously
166 from late Miocene until Present Day. This brings some contrasted interpretations about
167 whether thin- and thick-skinned deformation were simultaneous or diachronous. If the
168 deformation was simultaneous in the hangingwall and footwall (Eude et al. 2015, Calderon
169 et al. 2017b, 2017a), the presence of the thick *décollement* in the hangingwall of the
170 Chazuta Thrust sheet could have successfully decoupled the deformation between the two
171 blocks. Therefore, the component of deformation transmitted by the basement (thick-
172 skinned) deformation would have been absorbed entirely by the evaporitic *décollement*
173 and squeezed between both blocks. On the contrary, a diachronic scenario of deformation
174 may be based on the lack of deformation in the Chazuta Thrust sheet, suggesting that the
175 Chazuta Thrust formed after basement deformation took place.

176 The complexity of the basin geometry and the scarcity of seismic data make it difficult to
177 understand which mechanism(s) have led to the current geometry and kinematics of the
178 basin. Interpretation of seismic data is not sufficient to explain several aspects of the basin
179 and especially why the transport of the Chazuta Thrust is so large with a mostly non-
180 deformed hangingwall, a singularity at the scale of the Subandean zone and worldwide. The
181 main goal of this manuscript is to understand the conditions that have allowed an
182 overthrust to accommodate such a large quantity of horizontal displacement, and how such
183 a large evaporitic volume was able to be carried along with it.

184 ## 3 Analogue modeling methodology

185 ### *3.1 Material and scaling*

186 Our experimental approach focused on modeling a contractional tectonic wedge where
187 shortening could be accommodated continuously along one major frontal thrust. Our
188 models were of the pull-from-the-base type, as in Storti and McClay (1995). The base of the
189 sedimentary sequence was made of a viscous *décollement* of silicone polymer (SGM36,
190 manufactured by Dow Corning, UK), as in Costa and Vendeville (2004), Ferrer et al. (2014),
191 Sellier et al. (2013) and Weijermars and Schmeling (1986), which is a transparent, high-
192 viscosity polydimethylsiloxane (PDMS) polymer. Within the range of strain rates used
193 during the experiments (2×10^{-6} s^{-1}), PDMS behaves as a Newtonian fluid having a
194 negligible yield strength (Weijermars and Schmeling, 1986). Under these conditions, this is
195 a proper analogue for salt rock, or, in general, evaporites. The basal viscous *décollement*
196 was overlain by a brittle sedimentary cover made of dry quartz sand (GA39 and NE34, both
197 manufactured by Sibelco, France). GA39 sand was used to cover the viscous décollement
198 because it has a finer grain size than that of the NE34 sand. GA39 sand has a density of 1.42

199 g.cm^{-3}, a mean grain size of 127 μm and an internal frictional coefficient of about 0.69
200 (Klinkmüller et al., 2016). NE34 sand was used for the rest of the overburden. It has a
201 density of 1.65 g.cm^{-3}, a mean grain size of 220 μm and an internal friction coefficient of
202 about 0.6 (Table 1, Klinkmüller et al., 2016). Sand layers had different colors in order to
203 image sedimentary layering and faults, but had similar rheological behavior. In addition,
204 each layer interface was highlighted with a thin black marker.

205 Following the rules of scaling for tectonic experimental models (Hubbert, 1937; Ramberg,
206 1981), dry granular materials are good analogues for brittle sedimentary rocks in the
207 upper continental crust because they obey a Mohr-Coulomb criterion of failure (Hubbert,
208 1951; Krantz, 1991; Schellart, 2000; Lohrmann et al., 2003). Their angle of internal friction
209 is similar to natural rocks, and their cohesion can be, once scaled, considered to be
210 negligible. Scaling rules impose that the model-to-nature ratio for stress (imposed by the
211 ratio of the lithostatic pressure), σ*, should be:

212 $\sigma^* = \rho^* \times g^* \times L^*$ (Equation 1)

213 where ρ* is the model-to-nature ratio for volumetric mass, g* is the ratio for gravity
214 acceleration and L* is the ratio for length. L* is set to 0.66 x 10^{-5}, which means that 1 cm in
215 the model corresponds to 1.5 km in nature (Table 1). g* is 1 because the models were
216 deformed under a natural gravity field. The scaling ratio for density, ρ* is approximately
217 0.5. We used a volumetric mass of 2.6 g/cm^3 for natural clastic rocks, 2.2 g/cm^3 for halite,
218 1.4 and 1.6 g/cm^3 for the sands we used, and 0.965 g/cm^3 for the silicone polymer
219 (Weijermars et al., 1993; Santolaria et al., 2015). Considering these values, computed σ* is
220 3.33 x 10^{-6}. The cohesion value ranges of a few tens of Pascals for our granular materials,

which would corresponds to a value for natural sedimentary rocks in the range of 10-30 MPa, which is in good agreement with the scaling rules (Schellart, 2000).

For scaling viscosity and time, we took a dynamic viscosity for rocksalt of 5×10^{18} Pa.s (*e.g.* van Keken et al., 1993). This viscosity value was assumed from previously published data and not measured in this study. Note that estimated values for viscosity of natural rocksalt varies from 10^{16} and 10^{19} Pa.s (Carter, 1976; van Keken et al., 1993). If one considers another natural dynamic viscosity, it would drastically change the scaled natural velocity. The dynamic viscosity of the polymer we used is 2.2×10^{4} Pa.s (Rudolf et al., 2016). These values yield to a model-to-prototype ratio for viscosity η^* of 4.4×10^{-15}. The strain rate ratio, $\dot{\varepsilon}^*$, is linearly related to stress and viscosity ratios by the following equation:

$$\sigma^* = \eta^* \times \dot{\varepsilon}^* \quad \text{(Equation 2)}$$

Computing the strain rate yields to $\dot{\varepsilon}^* = 7.5 \times 10^{9}$, from which a model-to-nature time ratio can be quantified. As $t^* = 1/\dot{\varepsilon}^* = 1.33 \times 10^{-9}$, which means that one hour in the experiment is equivalent to about 85000 years in nature. As our experiments lasted around 65 hours, this represents around 5.6 My of deformation time in nature. Finally, we applied a convergence velocity of 5 mm/h in our model. This velocity, scaled to nature is:

$$v^* = \dot{\varepsilon}^* \times L^* \quad \text{(Equation 3)},$$

which corresponds to a velocity of about 9 mm/yr in nature.

3.2 Experimental setup and protocol

We carried out seven experiments in a deformation device at the Tectonic Modeling Laboratory of the University of Lille, France. The box was 85.5 cm long and 60 cm wide and was bounded by two fixed glass sidewalls and by two fixed wooden end walls. The base of

243 the deformation table was initially flat and covered by a linoleum sheet that was attached
244 to a mobile wall attached to a screw jack controlled by a stepper motor (Figure 7). The
245 basal linoleum sheet was able to move freely below the two fixed end-walls. Deformation
246 was imposed by pulling the basal sheet at a constant velocity of 0.5 cm/h. In some
247 experiments, the lateral friction along the glass sidewalls was decreased by lubricating
248 them with a film of silicone polymer (as in Costa and Vendeville, 2002; Santolaria et al.,
249 2015). This allowed reducing the influence of lateral friction during deformation. The
250 evolution of deformation was recorded by two CCD cameras (Figure 7) that shot
251 photographs every 30 minutes.

252 All models comprised a 60 cm wide, 65 cm long and 1.5 cm thick basal viscous *décollement*
253 made of viscous silicone polymer (Figure 8), except for the first model (Chaz_01) that
254 comprised a 1 cm thick polymer layer (Figure 8C, Table 2). The forelandwards edge of the
255 polymer is called here pinch-out (Figure 8B and 8C).

256 In our protocol, we tested the role of several parameters on the geometry and evolution of
257 deformation (Figure 8D, and Table 2). The tested parameters were mainly extracted from
258 the restored cross section of Calderon et al. (2017b, Figure 3). There, we observed that the
259 basal *décollement* is slightly tilted towards the foreland, and that the pre-tectonic
260 sedimentary cover lays parallel to the *décollement*. We first tested the impact of the
261 thickness of a tabular, pre-kinematic sedimentary cover (1.5 or 3 cm thick) and the tilting
262 of an initially flat basement (Figure 8C). In some experiments, the pre-kinematic cover was
263 completed by a sand wedge (Figure 8C, models Chaz_03 and 04). In the model Chaz_03
264 only, a sand wedge was deposited directly onto the basal *décollement* (Table 2). The idea
265 for adding an overburden wedge onto the system came from the cross-section restoration

of Calderon et al. (2017b) showing a thick Middle Eocene to Pliocene wedge at the rear of the Chazuta Thrust (yellow wedge in Figure 3). The presence of such wedge can alter the mechanical behavior and kinematic evolution of the evaporites and their overburden in two ways. First, the thickness of the brittle wedge decreases eastwards (towards the Chazuta thrust front), thereby decreasing its strength towards the foreland. Hence, it is the distal (thinnest) segment of the wedge that was most prone to fail first. As observed in other physical experiments, the proportionally thicker rear of the wedge did not deform (Smit et al., 2003). Second, deposition of a thick wedge on top of the evaporites would tend to cause the overburden to subside in the proximal region (rear part of the wedge), favoring forward evaporites flow and leading to evaporites inflation in the distal part (*e.g.* Wu et al., 2014). In our study area, evaporites inflation towards the foreland uplifted the overburden, allowing the Chazuta Thrust to incorporate the evaporites in the advancing allochthonous sheet and favoring a longer slip. This would also explain how such large volumes of evaporites can be found in an allochthonous position within the Chazuta thrust sheet. We tested the influence of surface processes in our experimental protocol by adding variable syn-kinematic sedimentary wedges having different thicknesses and tapering towards the foreland (Figure 8D; models Chaz_04, 05, 06 and 07). The front of the Chazuta Thrust was also subjected to erosion as observed in the seismic sections where cretaceous rocks crop out at the front of the thrust. In order to evaluate the role of erosion we eroded the deformation front in models Chaz_06 and Chaz_ 07. Finally, an episode of pre-kinematic deformation was tested by creating artificially an analogue of the Biabo Syncline that formed earlier, and was located on the hinterland side of the Chazuta Thrust (models Chaz_06 and 07). In order to generate artificially a pre-kinematic syncline, we deposited a

289 small, linear sand ridge (trending parallel to the *décollement* pinch-out) onto the
290 overburden. Under the sole effect of gravity, the local excess weight forced this narrow area
291 to subside and acquire the shape of a synform. As a result, a synform nearly grounded onto
292 the base of the viscous *décollement*, as did the Biabo Syncline in our study area.

293 All the models were shortened up to about 31 cm, which corresponds to 46.5 km in nature.
294 In this study, we compare the results of seven models that illustrate the impact of the
295 parameters mentioned above (alone or in combination) on the accommodation of the
296 deformation along one major thrust. We then compare these mechanisms and parameters
297 with the Chazuta Thrust in the Huallaga Basin.

298 *3.3 Strength profiles analysis*

299 The evolution of model deformation was recorded using top- and side-views photographs
300 that allowed producing movies (see supplementary material) suitable for an accurate
301 kinematical investigation. Analysis of strength profiles was also carried to quantify the bulk
302 strength of models and to compare the experimental results. In previous works, Bonini
303 (2001 and 2007) and Smit et al. (2003) discussed the effect on deformation style of relative
304 strength between the brittle overburden and a viscous *décollement*. Following the same
305 approach, we computed strength profiles of the initial conditions for each of our models
306 (Table 3 and Figure 9). When the thickness of the brittle overburden varied across-strike,
307 we computed two strength profiles that we called "min" and "max" (Table 3).

308 We first computed the vertical normal stress for the brittle overburden, which corresponds
309 to σ_3 for compressional regime, using:

310 $\sigma_3 = \rho \times g \times h$ (Equation 4),

where ρ is the mean density of the sand, g the acceleration of gravity, and h the thickness of the brittle overburden.

From the Mohr circle, we calculate the magnitude of σ_1 following :

$$\sigma_1 = \sigma_3 \times \left(1 \frac{2\sin\phi}{(1-\sin\phi)}\right) \quad \text{(Equation 5)},$$

where ϕ is the mean angle of internal friction for the material of the brittle overburden (Table 1). We used the differential stress to quantify the strength of the brittle overburden, computing $\sigma_1 - \sigma_3$.

Then, we computed the shear stress in the viscous layer (τ_d) to quantify the strength of the viscous *décollement*, using :

$$\tau_d = \eta \times \dot{\gamma} = \eta \times \frac{v}{h_d} \quad \text{(Equation 6)},$$

where η is the viscosity of the silicone polymer (Table 1) and $\dot{\gamma}$ is the shear strain rate, defined by the ratio between the backstop velocity v and the viscous *décollement* thickness h_d (Table1). One can note from Eq. 6 that the shear stress in the *décollement* is an inverse function of the thickness of the *décollement*. Therefore, for given backstop velocity and *décollement* viscosity, the *décollement* becomes stronger when its thickness decreases.

We then computed the ratio between the differential stress in the brittle overburden and the shear stress in the *décollement* ($R=(\sigma_1-\sigma_3)/\tau_d$). This stress ratio defines the brittle-ductile coupling (Allemand, 1988) and controls the distribution of deformation (distributed vs. localized) and the deformation style.

4 Experimental results

The evolution of deformation of each model is described based on its morphostructural evolution in map view. Side-view movies of each experiment are provided as supplementary material to this article. The final structure after shortening is illustrated in map view and by a cross section. Figure8 and Table 2 indicate the parameters tested for each model.

The magnitudes of stress are reported in Table 3. The strength profiles representing the differential stress for the brittle overburden and the shear stress for the décollement with respect to depth are illustrated for each model in Figure 9.

4.1 Model Chaz_01

The first model, Chaz_01 had a flat, horizontal basement, a 1 cm thick, tabular layer of viscous silicone polymer, and a 1.5 cm thick, tabular pre-kinematic brittle sand overburden. The sidewalls were lubricated (Table 2). The stress ratio for Chaz_01 (R_{Chaz_01}=173) is relatively small (Table 3, Figure 9).

Deformation nucleated at the *décollement* pinch-out (T_1), which acted as a major velocity discontinuity (Figure 9A). Subsequent thrusts and (T_2, to T_6) nucleated at the rear of the first thrust, leading to an "out-of-sequence" deformation style (Figure 10A to 10E, Supplementary material 1). In this model, the 31cm of shortening were accommodated by about six structures that partitioned the deformation. The majority of the thrusts were located at or near the front of the wedge (Figure 10), whereas the rear of the wedge was characterized by one detachment fold associated with a backthrust (B_9).

4.2 Model Chaz_02

In model Chaz_02, the thickness of the sand overburden was double of that in model Chaz_01 (from 1.5 to 3 cm), and the *décollement* thickness was increased from 1 to 1.5 cm

(Table 2), leading to a stress ratio three times higher (R_{Chaz_02}=519) than for Chaz_01 (Table 3, Figure 9).

Deformation initiated at the distal foreland pinch-out of the *décollement* with the formation of a thrust and a backthrust (T_1 and B_1, Figure 11A). Then, deformation along B_1 stopped and two near thrusts (T_2 and T_3) nucleated at the back of thrust T_1 in an "out-of-sequence" mode (Figure 11A to 11F, Supplementary material 2). At the end of the experiment, the wedge comprised three fault-related folds associated with thrusts located across the entire length of the wedge. As confirmed with the computation of the stress ratio, doubling the thickness of the sedimentary cover increased its strength, reducing the number of structures and increasing their wavelength (Figure 11G).

4.3 Model Chaz_03

In model Chaz_03, a sand wedge was deposited directly above an initially tabular viscous *décollement* layer before the onset of shortening. The deposition of the sand wedge was done after having tilted the base of the deformation box by 3 degrees (Table 2). Because of the deposition of the wedge, the initial stress ratio between the brittle overburden and the *décollement* varied across strike in this model (Figure 9). It was much smaller (by a factor of 7) at the wedge toe than near the backstop. In this experiment, the sidewalls were not lubricated to strengthen and test the frontal localization of deformation at the wedge toe.

Results indicate that the 31 cm of shortening were accommodated entirely along one single structure T_1 that nucleated at the distal pinch-out of the viscous *décollement* (Figure 12, Supplementary material 3). The top of the viscous *décollement* in the distal area was uplifted to a level higher than that of the thrust ramp, allowing some amount of the silicone polymer to be dragged forward along the thrust sheet (Figure 12G). A few small sand

blocks can be found embedded within the allochthonous polymer corresponding to overburden debris that formed superficially at the front of the thrust and became progressively overrun by the thrust sheet and its viscous sole. In this experiment, there was no erosion. In the center of the model, the segment of the frontal thrust located beyond the allochthonous viscous *décollement* eventually grounded to a halt, forcing the formation of a new backthrust (B_1) and hindering any further advance of the T_1 thrust sheet (Figure 12F).

4.4 Model Chaz_04

The boundary conditions for model Chaz_04 comprised a pre-kinematic 3 cm thick overburden overlain by a frictional wedge (Figure 8D, 13A and Table 2). This entailed two markedly different strength profiles across strike in the model (Figure 9). As for model Chaz_03, the stress ratio is higher near the backstop where the brittle overburden is thick and it is lower at the pre-kinematic wedge toe where the brittle overburden is thinner. Note that the value of the stress ratio at the wedge in Chaz_04 (R_{Chaz_04}=1057) is equal to the value of the stress ratio for Chaz_02 (Table 3).

Two syn-kinematic wedge-shaped units (the first one in blue, the second one in brown) were added during shortening (Figure 13B and 13E). As in the previous models, deformation initiated at the viscous *décollement* pinch-out by the formation of T_1 (Figure 13A). After deposition of the first syn-kinematic wedge, T_2 nucleated out of sequence near the sand-wedge pinch-out (Figure 13B, Supplementary material 4). At the final stage, this model showed three structures located at or near the front of the built wedge: two major thrusts and one minor one (Figure 13F and 13G). Compared with model Chaz_02 (Figure 11), in which deformation occurred across the entire length of the wedge, deformation in

400 the model Chaz_04 was restricted to the front of the wedge (Figure 13). These results
401 indicate clearly that by increasing progressively the overburden thickness at the back of
402 the model, this increased the stress ratio difference between the wedge front and its inner
403 part, and therefore lead pre- and syn-kinematic sedimentation to contribute to localize all
404 the deformation at the wedge toe. The toe of the wedge was thinner, hence easier to
405 deform. In both cases (models Chaz_02 and Chaz_04), an imbricate thrust system verging
406 towards the foreland formed, but the location and the geometry of the thrust system was
407 clearly different.

408 *4.5 Model Chaz_05*

409 The model Chaz_05 tested both syn-kinematic sedimentation above a thin (1.5 cm thick)
410 pre-kinematic cover, and syn-kinematic tilting (by 3°) of the model's base (Table 2). This
411 syn-kinematic tilt of the bow would correspond to a foreland flexure of the basin. In this
412 experiment, the glass sidewalls were not lubricated. The value of the stress ratio is constant
413 across strike and relatively low (R_{Chaz_05}=529), compared to previous models (Table 3,
414 Figure 9).

415 Deformation started with a compressional phase of a tabular overburden overlying a
416 tabular viscous *décollement*. Deformation initiated first at the viscous *décollement* pinch-
417 out by the formation of a thrust T_1 (Figure 14A). As deformation progressed, three later
418 structures (a thrust T_2 associated to a backthrust B_1, and a thrust T_3) formed at the back of
419 T_1 (Figure 14B). Then, the landward tilt of the basement and the onset of a flat-top syn-
420 kinematic sedimentary wedge (orange in Figure 14G) sealed temporarily the former
421 structures (thrusts T_1, B_1, T_2 and T_3) before that they were subsequently reactivated and
422 accommodated the rest of the shortening. Two last thrusts (thrusts T_4 and T_5) formed in an

423 "out-of-sequence" mode in the middle of the wedge during the last stages of shortening
424 (Figure 14D to 14F, Supplementary material 5). The structural style at the end of the
425 experiment is characterized by two major thrusts accommodating most of the shortening
426 (T_1 and T_3, Figure 14F and 14G), and by three second-order thrusts (T_2, T_4 and T_5). Once
427 again, syn-kinematic sedimentation helped to localize deformation at the front of the
428 wedge.

429 4.6 *Model Chaz_06*

430 In the previous models, the boundary conditions favored the localization of deformation at
431 the front of the wedge, but models having a pre-kinematic, tabular overburden ceased to
432 deform along one major thrust after a while, and deformation was distributed across the
433 models. With models Chaz_06 and Chaz_07, we tested the impact of the formation of an
434 early syncline (simulating the Biabo syncline in the Huallaga Basin), and how its presence
435 might have affected the thickening of the evaporites in the distal area, and consequently,
436 favoring overthrusting of the overburden, but also of the evaporites themselves. These two
437 models allowed computing two initial strength profiles across strike (Figure 9). The values
438 of the stress ratios are the same for both models because we did not vary the initial
439 thickness of the overburden and *décollement*. The smallest stress ratio corresponds to the
440 one of Chaz_05.

441 Model Chaz_06 comprised a flat and 1.5 cm thick sedimentary cover that overlay a 1.5 cm
442 thick viscous *décollement* (Table 2). A sand ridge was deposited at 28 cm from the internal
443 backstop (Figure 15A). Compression started after an early subsidence of the ridge that
444 created a synform. Deformation started at the distal viscous *décollement* pinch-out by the
445 formation of thrust T_1. Then, a minor backthrust B_1 formed on the flank of the synform

(Figure 15A). Deposition of the first syn-kinematic sand wedge (green in overhead views) sealed B_1 (Figure 15B). The two former structures (T_1 and B_1) were then reactivated, and no new fault appeared (Figure 15B to 15D, Supplementary material 6). Deposition of the second syn-kinematic sand wedge (brown in overhead view), combined with an episode of erosion of the deformation front (by vacuuming the sand that had collapsed in front of the frontal thrust) inhibited the subsequent growth of backthrust B_1, fossilizing this structure (Figure 15E). The main frontal thrust T_1 accommodated all the shortening, favoring the inflation of the distal viscous *décollement* and thus arching and lifting the overburden. The initial position of the early synform close to that of the *décollement* pinch-out led them to collide during the last stages of the experiment. During these last stages, the distal viscous *décollement* thickened, uplifted its overburden, creating an open toe. The viscous *décollement* reached the surface and spread locally onto the foreland's surface (Figure 15F). The system being locked, no more viscous *décollement* was able to inflate, and propagation of the frontal thrust was made less easy. Finally, this experiment indicates that the presence of an early syncline allowed for a thick volume of allochthonous viscous *décollement* to rise above the thrust ramp (Figure 15G).

4.7 Model Chaz_07

In order to constrain the role of a pre-kinematic syncline located farther away from the viscous *décollement* pinch-out, one last model (model Chaz_07, Figure 16) was carried out. This experiment had a configuration similar to that of the previous model (Chaz_06, Figure 15 and Table 2) except for the fact that the ridge was positioned further behind, at 18 cm from the internal backstop. At the onset of the experiment, the base of the model was totally flat and deformation started by a thrust (T_1) located at the viscous *décollement*

469 pinch-out, then was followed by the formation of a minor thrust T_2, located at the back of
470 the ridge (Figure 16A). A third thrust T_3 nucleated at the rear of T_1, just before the episode
471 of syn-kinematic sedimentation. It is incipient in Figure 15A. Subsequently, the base of the
472 deformation box was tilted landward, and a thick sedimentary wedge was added (green)
473 sealing T_2 and T_3 (Figure 16B, Supplementary material 7). Thrust T_1 continued to
474 accommodate shortening. Slip along T_1 was favored by erosion of the deformation front
475 during the whole shortening, helped by the fact that some viscous polymer was dragged
476 above the ramp along with the thrust sheet (Figure 16B to 16F). The final cross section in
477 this model shows that deformation was essentially accommodated at the front of the wedge
478 along one single fault plane (T_1). Thrust T_1 remained active during the whole compression
479 and accommodated the major part of shortening (Figure 16G). The combined effect of
480 wedge-shaped sedimentation, and the bulldozing effect produced by the presence of the
481 early synform forced the viscous *décollement* to thicken distally and hence to move upward
482 and forward along with the frontal thrust. The new location of the syncline enabled the
483 forward "bulldozing" effect, uplifting more volume of the viscous *décollement* than in the
484 Chaz_06 model. The combination of syn-kinematic erosion, sedimentation and the presence
485 of an early syncline located in the back led to the formation of a wedge where only one
486 major, long-lived thrust accommodated the entire shortening and brought some of the
487 viscous *décollement* into the hangingwall.

488 **5 Discussion**

489 The goal of this study was to decipher which parameters may have had the most significant
490 influence on favoring the remarkable characteristics of the Chazuta Thrust (Huallaga Basin,
491 Peru), that has (1) a large amount of slip along one single frontal structure, (2) a

surprisingly intact allochthonous sedimentary series showing little or no deformation, and (3) the emplacement of a large volume of initially autochthonous evaporites passively dragged upward in an allochthonous position along with the thrust sheet. In this section, we first discuss the impact of the tested parameters on the structure of fold-and-thrust belts. We then give the insights that our models provide to better understand the formation of the Chazuta Thrust.

5.1 Impact of the initial sedimentary cover thickness

The first group of models (Chaz_01 and Chaz_02) tested the influence of the thickness of a tabular pre-kinematic sedimentary cover on the structural style and evolution of a fold-and-thrust belt. Between models Chaz_01 to Chaz_02, we doubled the thickness of this cover. Such thickening increased the cover strength and reduced the number of structures and their wavelength (compare Figure 10F with Figure 11G). This is in good agreement with already published works for frictional and frictional-viscous wedges (Huiqi et al., 1992; Marshak and Wilkerson, 1992; Smit et al., 2003; Storti et al., 2007). The sidewalls of the models being lubricated, this helped the structures to propagate rapidly across the whole length of the model up to the *décollement* pinch-out.

5.2 Impact of pre- or syn-kinematic sedimentation and basal slope

The second group of experiments comprised three models (Chaz_03, Chaz_04 and Chaz_05), that tested the impact of a sedimentary wedge, either pre-kinematic (Chaz_03 model) or syn-kinematic (Chaz_04 and Chaz_05 models, respectively), on the kinematics of the deformation front. These models also tested the effect of tilting the basal *décollement* of the wedge towards the hinterland on the deformation.

514 Model Chaz_03, comprising a pre-kinematic wedge and a tilted basement, showed that only
515 one structure accommodated the whole shortening. At the end of shortening, a new
516 backthrust formed, preventing any further advance of the thrust sheet (Figure 12F). Had
517 the distal front of the thrust sheet been subjected to erosion, the allochthonous *décollement*
518 might have ended up cropping out, allowing for much more advance of the allochthonous
519 system (Merle and Abidi, 1995). Additionally, the absence of sidewall lubrication also
520 favored the localization of deformation along one single structure.

521 The other two models from this group (Chaz_04 and Chaz_05) tested a similar effect, but
522 with the presence of a pre-existing, tabular overburden (corresponding to Late Jurassic to
523 early Eocene in the study area). Results indicate also that syn-kinematic sedimentation
524 increased the thickness at the back of the wedge, hence its strength. This helped localizing
525 deformation at the front of the wedge because the overburden was thinner there and easier
526 to deform (Figure 13G and Figure 13G).

527 In summary, this group of three experiments highlights that the presence of an overburden
528 wedge with or without a basal slope favors a longer activity of the thrusts in the distal area,
529 at or near the *décollement* pinch-out. In models having an initial tabular overburden under
530 the sedimentary wedge (Chaz_04 and Chaz_05), the frontal thrust formed first, then was
531 followed by new structures behind it. As Merle and Abidi (1995) observed, this behavior is
532 explained by the fact that displacement along the frontal thrust was becoming more and
533 more difficult as the frontal thrust slipped forward. The overburden that had to be carried
534 forward along the distal front became so thick so that the frontal thrust progressively
535 became locked, forming a frontal buttress, and forcing new thrusts to nucleate landward. In
536 these models, only a thin sliver of silicone was transported along with the thrust sheet in an

allochthonous position (Figure 13G and Figure 14G). Therefore, it is not obvious that the top of the silicone layer was raised much above the thrust-ramp level.

5.3 Influence of early deformation and syn-kinematic erosion-sedimentation

In the previously discussed models, the boundary conditions favored the localization of deformation at the front of the wedge, but models having a pre-kinematic, tabular overburden ceased to deform along one major frontal thrust after a while. With this last set of models, we tested the impact of the presence of an early synform and how it might have favored the thickening of the viscous *décollement* in the distal area, and consequently, helping its overthrusting.

Although the Biabo Syncline located at the back of the Chazuta Thrust was present before the formation of the Chazuta Thrust (see Middle Eocene stage in Figure 3), our goal was not to model the causes of its formation, but rather to evaluate how its presence might have impacted on the evolution of the overall system, and particularly on the kinematics of deformation at the frontal salt pinch-out. Typically, during thin-skinned shortening above an evaporitic layer, anticlines rise, whereas synclines subside deeply within the evaporitic layer, often grounding onto the base of the evaporites (*e.g.* Costa and Vendeville, 2002; Cotton and Koyi, 2000). During ongoing shortening, the distal evaporites bulldozed by the grounded syncline are pushed forward and forced to thicken up to the point that their top exceeds the height of the frontal thrust ramp. When this occurs it makes it possible for the evaporites to spill forward onto the foreland, locally developing salt sheets, such can be observed in the Fars region in Iran (*e.g.* Hudec and Jackson, 2006).

In Chaz_06, the combination of wedge-shaped syn-kinematic sedimentation and the bulldozing effect created by the early syncline helped the viscous *décollement* to inflate and

560 hence to be incorporated into the frontal thrust. However, the initial location of the early
561 synform was too close to that of the *décollement* pinch-out. The anticline and the distal
562 ramp eventually collided during shortening, locking the system and blocking any further
563 propagation of the frontal thrust (Figure 15). With the model Chaz_07, we show that the
564 combination of syn-kinematic erosion/sedimentation and the presence of an early syncline
565 located farther away at the back of the model, led to the formation of a wedge where a long-
566 lived major thrust accommodated the major amount of the shortening, and incorporated
567 some viscous *décollement* in its hangingwall (Figure 16).

568 *5.4 Strength profiles analysis*

569 The overall structural style (distributed vs. localized strain) of a fold-and-thrust belt
570 detaching over a viscous *décollement*, depends on the relative strength between the brittle
571 overburden and the viscous *décollement* (e.g. Allemand, 1988; Bonini, 2001; Smit et al.,
572 2003). For instance, a viscous layer tends to deform internally with distributed strain. In
573 contrast, a brittle overburden tends to undergo localized deformation along fault planes or
574 shear zones, with little or no internal strain between the faults. Had the viscous layer been
575 stronger than the brittle one, strain in both layers would have been widely distributed
576 throughout the model, and many faults would have formed in the upper sand layer.

577 All the initial strength profiles of our models show the same trend (Figure 9). In every
578 models, the differential stress of the brittle overburden is much larger than the shear stress
579 of the *décollement*. This clearly indicates that the brittle overburden is overwhelmingly (by
580 orders of magnitude) stronger than the décollement. Therefore, we can confidently state
581 that during our experiments, the overall structural style and evolution are nearly entirely
582 dictated by deformation of the brittle overburden, while the role of viscous *décollement* is

merely to accommodate the displacements of the upper sand layer, which deforms along only few thrust.

The differential stress of the overburden is 87 to about 870 times bigger than the shear stress (Table 3) which explains differences in the localization of deformation. The relatively small initial stress ratio in Chaz_01 led to localize the deformation along more structures than in Chaz_02, which had a bigger initial stress ratio. This is in agreement with the results of Smit et al. (2003) who state that the structural style is controlled by the relative strength between the *décollement* and the cover. In the last models of our study, the values of initial stress ratios confirm that the distribution of deformation along the wedge is function of the strength in the brittle overburden. Increasing the strength at the back of the wedge allowed localizing deformation at the frontal part of the wedge.

5.5 Insights for the Chazuta Thrust in the Huallaga Basin

The cross section restored by Calderon et al. (2017b) shows that the Huallaga Basin had several distinctive characteristics worth investigating. We tested, using a series of analogue experiments, the impact of several parameters that are present in the Chazuta Thrust. We compared our results with this thrust's present-day and restored cross sections in order to better understand its geometry and kinematics. The Huallaga Basin presents a tabular pre-kinematic sedimentary cover (from late Permian to Paleocene) and thick Eocene to Neogene syntectonic series, especially in the Biabo Syncline (Figure 3).

Our models indicate that the presence of a syn-kinematic wedge above a tabular cover contributes to localize the deformation at the front of the wedge. However it is not sufficient to generate a long-lived thrust that incorporates a large volume of evaporites in its hangingwall, such as in the case of the Chazuta Thrust in the center part of the basin. In

606 order to obtain such a peculiar geometry, experimental results show that the wedge needs
607 a locally thicker syn-kinematic proximal series and erosion of the deformation front.

608 The cross sections in the last two experimental models (Chaz_06 and Chaz_07) can be
609 compared with those across the Chazuta Thrust. In the models, the synform that formed by
610 the early subsidence of the sand ridges contributed to push the viscous *décollement* above
611 the front of the wedge. Particularly, in model Chaz_07, the combination of the early
612 formation of a synform and erosion of the deformation front during shortening led to the
613 formation of a thrust that accommodated the major part of shortening. We believe that
614 comparable processes have happened in the Huallaga Basin with the Biabo Syncline that
615 pushed the evaporites towards the frontal part of the belt. Erosion of the Chazuta
616 deformation front, as indicated by truncated reflectors on the seismic lines (Figure 4)
617 helped the Chazuta Thrust to accommodate very significant amounts of shortening with
618 little or no deformation of the hangingwall.

619 In the northern and southern parts of the Huallaga Basin, the geometry of the Chazuta
620 Thrust is slightly different compared to the center part of the basin. In the North, the thrust
621 sheet is offset by a backthrust at the front of the Biabo Syncline and by minor thrusts that
622 root in the allochtonous *décollement* (Figure 5). In the South, the Chazuta thrust sheet is
623 deformed by a pop-up structure (Figure 6). Our set of analogue models did not intend to
624 explain these lateral variations, but some hypothesis can be made about them. For instance,
625 these variations could be explained by along-strike variation of evaporites distribution
626 and/or facies (*e.g*. Bahroudi and Koyi, 2003). The northern and southern parts of the basin
627 seem to correspond to the limit of the evaporites area. The deformation in these parts of

628 the basin could also be impacted by edge effects along the adjacent areas that do not have
629 an evaporitic *décollement* (e.g. Zhou et al., 2016; Borderie et al., 2018).

630 **6 Conclusions**

631 We carried out a series of analogue experiments in order to understand the major
632 geological parameters that have controlled the geometry and kinematics of the Chazuta
633 Thrust (Huallaga Basin, Peru). This thrust accommodates an important amount of
634 shortening and incorporates in its hangingwall an unusual large volume of the evaporitic
635 *décollement* material. We tested different parameters, such as the presence of a tabular
636 overburden, a syn-kinematic sedimentary wedge whose frontal tip lay near the frontal
637 thrust and erosion at the front of wedge. The basement slope at the base of the viscous
638 *décollement* layer. We also investigated the role of an early formed synform located at the
639 back of the frontal thrust were. The major results are the following.

640 (1) A system comprising a tabular viscous *décollement* and a tabular overburden cannot
641 generate a large amount of slip along a frontal thrust because this thrust is quickly
642 deactivated in favor of new thrusts forming at the back of it.

643 (2) Deposition of a pre- or syn-kinematic wedge of above the system helps nucleating
644 thrusts at the frontal pinch-out of the viscous *décollement*. The presence of a
645 sedimentary wedge favors a forward flow of the viscous *décollement.* This leads the
646 *décollement* to thicken and to reach an elevation higher than that of the footwall
647 ramp. The incorporation of some volume of viscous *décollement* within the
648 allochthonous system is favored, and thereby the duration in activity of the frontal
649 structure increases.

(3) The presence or absence of a slope at the base of the viscous *décollement* does not appear to have any major impact on the activity of the frontal thrust.

(4) The formation of an early syncline whose base rests near or on the base of the viscous *décollement* enhances distal *décollement* inflation. The syncline pushes forward the distal *décollement* during its advance, forcing it to inflate. This allows for the emplacement of allochthonous viscous *décollement* incorporated to the thrust system.

(5) Finally, the role of frontal erosion seems to be another key parameter. Without it, the debris in front of the thrust tend to accumulate and eventually act as a buttress that would block its activity.

On the basis of our experimental results, we believe that it is the particular combination of most (if not all) of the above parameters that contributed to the exceptional longevity of the Chazuta Thrust, its little inner deformation in the central part of the system and its very large horizontal displacement.

Acknowledgments

This work has been carried out during Sandra Borderie's Ph.D. at the University of Lille, with funding from the French Ministry of Research. Figure 1 and 2 were drawn using the software package GMT (Wessel and Smith, 1991). HIS Markit is kindly thanked for Academic Licenses of the Kingdom software. The authors thank PERUPETRO for providing the seismic data and the IRD-PERUPETRO Research agreement to allow us working in Lima. Gonzalo Zamora and Oriol Ferre are kindly thanked for his constructive advices on a

previous version of the paper. Marco Bonini is thanked for his useful comments on this version.

References

Allemand, P., 1988. Approche expérimentale de la mécanique du rifting continental. Sciences de la Terre. Université Rennes 1.

Amery, G., 1969. Structure of Sigsbee scarp, Gulf of Mexico. AAPG Bulletin 53, 2480–2482.

Bahroudi, A., Koyi, H., 2003. Effect of spatial distribution of Hormuz salt on deformation style in the Zagros fold and thrust belt: an analogue modelling approach. Journal of the Geological Society 160, 719–733.

Bergen, K.J., Shaw, J.H., 2010. Displacement profiles and displacement-length scaling relationships of thrust faults constrained by seismic-reflection data. Geological Society of America Bulletin 122, 1209–1219.

Billings, M.P., 1954. Structural geology, 2d ed., New York, Prentice-Hall. ed.

Bonini, M., 2007. Deformation patterns and structural vergence in brittle–ductile thrust wedges: An additional analogue modelling perspective. Journal of Structural Geology 29, 141–158. https://doi.org/10.1016/j.jsg.2006.06.012

Bonini, M., 2001. Passive roof thrusting and forelandward fold propagation in scaled brittle-ductile physical models of thrust wedges. Journal of Geophysical Research: Solid Earth 106, 2291–2311.

Bonnet, C., Malavieille, J., Mosar, J., 2008. Surface processes versus kinematics of thrust belts: impact on rates of erosion, sedimentation, and exhumation–Insights from analogue models. Bulletin de La Société Géologique de France 179, 297–314.

Borderie, S., Graveleau, F., Witt, C., Vendeville, B.C., 2018. Impact of an interbedded viscous décollement on the structural and kinematic coupling in fold-and-thrust belts: Insights from analogue modeling. Tectonophysics 722, 118–137. https://doi.org/10.1016/j.tecto.2017.10.019

Boyer, S.E., 1995. Sedimentary basin taper as a factor controlling the geometry and advance of thrust belts. American Journal of Science 295, 1220–1254.

Buiter, S.J.H., 2012. A review of brittle compressional wedge models. Tectonophysics 530–531, 1–17. https://doi.org/10.1016/j.tecto.2011.12.018

Calderon, Y., Baby, P., Hurtado, C., Brusset, S., 2017a. Thrust tectonics in the Andean retro-foreland basin of northern Peru: Permian inheritances and petroleum implications. Marine and Petroleum Geology 82, 238–250. https://doi.org/10.1016/j.marpetgeo.2017.02.009

Calderon, Y., Vela, Y., Hurtado, C., Bolaños, R., Baby, P., Eude, A., Roddaz, M., Brusset, S., Calvès, G., 2017b. Petroleum Systems Restoration of the Huallaga—Marañon Andean Retroforeland Basin, Peru. AAPG Memoir 114, 95–116. https://doi.org/10.1306/13602026M1143702

Carter, N.L., 1976. Steady state flow of rocks. Reviews of Geophysics 14, 301–360.

Costa, E., Vendeville, B.C., 2004. Experimental insights on the geometry and kinematics of fold-and-thrust belts above weak, viscous evaporitic décollement: reply to comments by Hemin Koyi and James Cotton. Journal of Structural Geology 26, 2139–2141. https://doi.org/10.1016/j.jsg.2004.04.001

Costa, E., Vendeville, B.C., 2002. Experimental insights on the geometry and kinematics of fold-and-thrust belts above weak, viscous evaporitic décollement. Journal of Structural Geology 24, 1729–1739.

Cotton, J.T., Koyi, H.A., 2000. Modeling of thrust fronts above ductile and frictional detachments: application to structures in the Salt Range and Potwar Plateau, Pakistan. Geological Society of America Bulletin 112, 351–363.

716 Coward, M., Kim, J., Parke, J., 1980. A correlation of Lewisian structures and their displacement across
717 the lower thrusts of the Moine thrust zone, NW Scotland. Proceedings of the Geologists'
718 Association 91, 327–337.
719 Cruz, L., Malinski, J., Wilson, A., Take, W.A., Hilley, G., 2010. Erosional control of the kinematics and
720 geometry of fold-and-thrust belts imaged in a physical and numerical sandbox. Journal of
721 Geophysical Research 115. https://doi.org/10.1029/2010JB007472
722 Dahlen, F.A., 1990. Critical Taper Model of Fold-And-Thrust Belts and Accretionary Wedges. Annual
723 Review of Earth and Planetary Sciences 18, 55–99.
724 https://doi.org/10.1146/annurev.ea.18.050190.000415
725 DeCelles, P.G., Giles, K.A., 1996. Foreland basin systems. Basin Research 8, 105–123.
726 Espurt, N., Brusset, S., Baby, P., Hermoza, W., Bolaños, R., Uyen, D., Déramond, J., 2008. Paleozoic
727 structural controls on shortening transfer in the Subandean foreland thrust system, Ene and
728 southern Ucayali basins, Peru: SHORTENING TRANSFER IN THE UCAYALI BASIN.
729 Tectonics 27, n/a-n/a. https://doi.org/10.1029/2007TC002238
730 Eude, A., Roddaz, M., Brichau, S., Brusset, S., Calderon, Y., Baby, P., Soula, J.-C., 2015. Controls on
731 timing of exhumation and deformation in the northern Peruvian eastern Andean wedge as inferred
732 from low-temperature thermochronology and balanced cross section: exhumation and
733 deformation of north Peru. Tectonics 34, 715–730. https://doi.org/10.1002/2014TC003641
734 Ferrer, O., Roca, E., Vendeville, B.C., 2014. The role of salt layers in the hangingwall deformation of
735 kinked-planar extensional faults: Insights from 3D analogue models and comparison with the
736 Parentis Basin. Tectonophysics 636, 338–350. https://doi.org/10.1016/j.tecto.2014.09.013
737 Fillon, C., Huismans, R.S., van der Beek, P., 2013. Syntectonic sedimentation effects on the growth of
738 fold-and-thrust belts. Geology 41, 83–86.
739 Gil Rodriguez, W., Baby, P., Ballard, J.-F., 2001. Structure et contrôle paléogéographique de la zone
740 subandine péruvienne. Comptes Rendus de l'Académie Des Sciences - Series IIA - Earth and
741 Planetary Science 333, 741–748. https://doi.org/10.1016/S1251-8050(01)01693-7
742 Gil Rodriguez, W.F.G., 2001. Evolution latérale de la déformation d'un front orogénique: Exemple des
743 bassins subandins entre 0 et 16 S. Université Toulouse III Paul Sabatier (UT3 Paul Sabatier).
744 Graveleau, F., Malavieille, J., Dominguez, S., 2012. Experimental modelling of orogenic wedges: A
745 review. Tectonophysics 538–540, 1–66. https://doi.org/10.1016/j.tecto.2012.01.027
746 Grelaud, S., Sassi, W., de Lamotte, D.F., Jaswal, T., Roure, F., 2002. Kinematics of eastern Salt Range
747 and South Potwar Basin (Pakistan): a new scenario. Marine and Petroleum Geology 19, 1127–
748 1139. https://doi.org/10.1016/S0264-8172(02)00121-6
749 Hermoza, W., Brusset, S., Baby, P., Gil, W., Roddaz, M., Guerrero, N., Bolaños, R., 2005. The Huallaga
750 foreland basin evolution: Thrust propagation in a deltaic environment, northern Peruvian Andes.
751 Journal of South American Earth Sciences, Cenozoic Andean Basin Evolution 19, 21–34.
752 https://doi.org/10.1016/j.jsames.2004.06.005
753 Hubbert, M.K., 1951. Mechanical basis for certain familiar geologic structures. Geological Society of
754 America Bulletin 62, 355–372.
755 Hubbert, M.K., 1937. Theory of scale models as applied to the study of geologic structures. Geological
756 Society of America Bulletin 48, 1459–1520.
757 Hubbert, M.K., Rubey, W.W., 1959. Role of fluid pressure in mechanics of overthrust faulting I.
758 Mechanics of fluid-filled porous solids and its application to overthrust faulting. Geological
759 Society of America Bulletin 70, 115–166.
760 Hudec, M.R., Jackson, M.P.A., 2006. Advance of allochthonous salt sheets in passive margins and
761 orogens. AAPG Bulletin 90, 1535–1564. https://doi.org/10.1306/05080605143
762 Huiqi, L., McClay, K., Powell, D., 1992. Physical models of thrust wedges. Thrust Tectonics. Springer,
763 71–81.
764 Kim, Y.-S., Sanderson, D.J., 2005. The relationship between displacement and length of faults: a review.
765 Earth-Science Reviews 68, 317–334. https://doi.org/10.1016/j.earscirev.2004.06.003

766 Kley, J., Monaldi, C.R., Salfity, J.A., 1999. Along-strike segmentation of the Andean foreland: causes
767 and consequences. Tectonophysics 301, 75–94.
768 Klinkmüller, M., Schreurs, G., Rosenau, M., Kemnitz, H., 2016. Properties of granular analogue model
769 materials: A community wide survey. Special Issue on GeoMod 2014 – Modelling in Geoscience
770 684, 23–38. https://doi.org/10.1016/j.tecto.2016.01.017
771 Koyi, H.A., Hessami, K., Teixell, A., 2000. Epicenter distribution and magnitude of earthquakes in fold-
772 thrust belts: insights from sandbox models. Geophysical Research Letters 27, 273–276.
773 Krantz, R.W., 1991. Measurements of friction coefficients and cohesion for faulting and fault reactivation
774 in laboratory models using sand and sand mixtures. Tectonophysics 188, 203–207.
775 Lacquement, F., Mansy, J.-L., Hanot, F., Meilliez, F., 1999. Retraitement et interprétation d'un profil
776 sismique pétrolier méridien au travers du Massif paléozoïque ardennais (Nord de la France).
777 Comptes Rendus de l'Académie Des Sciences-Series IIA-Earth and Planetary Science 329, 471–
778 477.
779 Lohrmann, J., Kukowski, N., Adam, J., Oncken, O., 2003. The impact of analogue material properties on
780 the geometry, kinematics, and dynamics of convergent sand wedges. Journal of Structural
781 Geology 25, 1691–1711.
782 Macedo, J., Marshak, S., 1999. Controls on the geometry of fold-thrust belt salients. Geological Society
783 of America Bulletin 111, 1808–1822.
784 Macellari, C., Hermoza, W., 2009. Subandean segmentation and its impact on hydrocarbon exploration in
785 the Central/Northern Andes. 10th Simposio Bolivariano-Exploracion Petrolera En Las Cuencas
786 Subandinas.
787 Marshak, S., Wilkerson, M.S., 1992. Effect of overburden thickness on thrust belt geometry and
788 development. Tectonics 11, 560–566.
789 McClay, K.R., Whitehouse, P.S., 2004. Analog modeling of doubly vergent thrust wedges. AAPG
790 Memoir 82, 184–206.
791 McGroder, M.F., Lease, R.O., Pearson, D.M., 2015. Along-strike variation in structural styles and
792 hydrocarbon occurrences, Subandean fold-and-thrust belt and inner foreland, Colombia to
793 Argentina. Geological Society of America Memoirs 212, 79–113.
794 McQuarrie, N., Ehlers, T.A., Barnes, J.B., Meade, B., 2008. Temporal variation in climate and tectonic
795 coupling in the central Andes. Geology 36, 999–1002.
796 Merle, O., Abidi, N., 1995. Approche expérimentale du fonctionnement des rampes émergentes. Bulletin
797 de La Société Géologique de France 166, 439–450.
798 Mugnier, J.L., Baby, P., Colletta, B., Vinour, P., Bale, P., Leturmy, P., 1997. Thrust geometry controlled
799 by erosion and sedimentation: A view from analogue models. Geology 25, 427–430.
800 Nelson, T., 1991. Salt tectonics and listric-normal faulting. The Gulf of Mexico Basin: Geological Society
801 of America, The Geology of North America, v. J 73–89.
802 Peel, F., Travis, C., Hossack, J., 1995. Genetic structural provinces and salt tectonics of the Cenozoic
803 offshore US Gulf of Mexico: A preliminary analysis.
804 Ramberg, H., 1981. Gravity, deformation, and the earth's crust: In theory, experiments, and geological
805 application. Academic press.
806 Ramos, V.A., 2010. The tectonic regime along the Andes: Present-day and Mesozoic regimes. Geological
807 Journal 45, 2–25. https://doi.org/10.1002/gj.1193
808 Ramos, V.A., Folguera, A., 2009. Andean flat-slab subduction through time. Geological Society, London,
809 Special Publications 327, 31–54. https://doi.org/10.1144/SP327.3
810 Rowan, M.G., 1995. Structural styles and evolution of allochthonous salt, central Louisiana outer shelf
811 and upper slope.
812 Rudolf, M., Boutelier, D., Rosenau, M., Schreurs, G., Oncken, O., 2016. Rheological benchmark of
813 silicone oils used for analog modeling of short-and long-term lithospheric deformation.
814 Tectonophysics 684, 12–22.

Santolaria, P., Vendeville, B.C., Graveleau, F., Soto, R., Casas-Sainz, A., 2015. Double evaporitic décollements: Influence of pinch-out overlapping in experimental thrust wedges. Journal of Structural Geology 76, 35–51. https://doi.org/10.1016/j.jsg.2015.04.002

Schellart, W., 2000. Shear test results for cohesion and friction coefficients for different granular materials: scaling implications for their usage in analogue modelling. Tectonophysics 324, 1–16.

Sellier, N.C., Vendeville, B.C., Loncke, L., 2013. Post-Messinian evolution of the Florence Rise area (Western Cyprus Arc) Part II: Experimental modeling. Basin Dynamics 591, 143–151. https://doi.org/10.1016/j.tecto.2011.07.003

Simpson, G.D., 2006. Modelling interactions between fold–thrust belt deformation, foreland flexure and surface mass transport. Basin Research 18, 125–143.

Smit, J.H.W., Brun, J.-P., Sokoutis, D., 2003. Deformation of brittle-ductile thrust wedges in experiments and nature. Journal of Geophysical Research 108. https://doi.org/10.1029/2002JB002190

Stockmal, G.S., Beaumont, C., Nguyen, M., Lee, B., 2007. Mechanics of thin-skinned fold-and-thrust belts: Insights from numerical models. Geological Society of America Special Papers 433, 63–98.

Storti, F., Marín, R.S., Rossetti, F., Sainz, A.C., 2007. Evolution of experimental thrust wedges accreted from along-strike tapered, silicone-floored multilayers. Journal of the Geological Society 164, 73–85.

Storti, F., McClay, K., 1995. Influence of syntectonic sedimentation on thrust wedges in analogue models. Geology 23, 999–1002.

Suppe, J., 2014. Fluid overpressures and strength of the sedimentary upper crust. Journal of Structural Geology 69, 481–492.

Suppe, J., 2007. Absolute fault and crustal strength from wedge tapers. Geology 35, 1127–1130.

van Keken, P.E., Spiers, C.J., van den Berg, A.P., Muyzert, E.J., 1993. The effective viscosity of rocksalt: implementation of steady-state creep laws in numerical models of salt diapirism. Tectonophysics 225, 457–476. https://doi.org/10.1016/0040-1951(93)90310-G

Wang, X., Suppe, J., Liang, H., He, D., 2014. Large-scale thrusting along the northern margin of the Tibetan Plateau and the southwest Tarim basin: 230 km long active Hotian thrust sheet. Presented at the EGU General Assembly Conference Abstracts.

Weijermars, R., Jackson, M., Vendeville, B., 1993. Rheological and tectonic modeling of salt provinces. Tectonophysics 217, 143–174.

Weijermars, R., Schmeling, H., 1986. Scaling of Newtonian and non-Newtonian fluid dynamics without inertia for quantitative modelling of rock flow due to gravity (including the concept of rheological similarity). Physics of the Earth and Planetary Interiors 43, 316–330. https://doi.org/10.1016/0031-9201(86)90021-X

Whipple, K.X., 2009. The influence of climate on the tectonic evolution of mountain belts. Nature Geoscience 2, 97–104.

Willett, S., Beaumont, C., Fullsack, P., 1993. Mechanical model for the tectonics of doubly vergent compressional orogens. Geology 21, 371–374.

Wine, G., Vetrici, D., Arcuri, J., Martinez, E., Monges, C., Fernandez, J., Calderon, Y., Galdos, C., 2001. The Huallaga basin and adjacent area, The hydrocarbon potential of NE Peru Huallaga, Santiago and Marañon Basins Study. Proyecto de Asistencia para la Reglamentacion del Sector Energetico del Peru.

Worrall, D., Snelson, S., 1989. Evolution of the northern Gulf of Mexico. The Geology of North America; an Overview: Geological Society of America, v. A 97–138.

Wu, J.E., McClay, K.R., 2011. Two-dimensional analog modeling of fold and thrust belts: dynamic interactions with syncontractional sedimentation and erosion. Thrust Fault-Related Folding AAPG Memoir 94, 301–333.

Wu, S., Bally, A.W., Cramez, C., 1990a. Allochthonous salt, structure and stratigraphy of the north-eastern Gulf of Mexico. Part II: Structure. Marine and Petroleum Geology 7, 334–370.

Wu, S., Vail, P.R., Cramez, C., 1990b. Allochthonous salt, structure and stratigraphy of the north-eastern Gulf of Mexico. Part I: Stratigraphy. Marine and Petroleum Geology 7, 318–333.

Wu, Z., Yin, H., Wang, X., Zhao, B., Jia, D., 2014. Characteristics and deformation mechanism of salt-related structures in the western Kuqa depression, Tarim basin: Insights from scaled sandbox modeling. Tectonophysics 612–613, 81–96. https://doi.org/10.1016/j.tecto.2013.11.040

Zhou, J., Zhang, B., Xu, Q., 2016. Effects of lateral friction on the structural evolution of fold-and-thrust belts: Insights from sandbox experiments with implications for the origin of landward-vergent thrust wedges in Cascadia. Geological Society of America Bulletin 128, B31320.1. https://doi.org/10.1130/B31320.1

Figure captions

Figure 1: Topographic map of Peru illustrating the location of the Eastern Cordillera, the Subandean zone, and the main foreland basins of the Subandean zone. The study area (Huallaga Basin) is marked by the red square. Topographic dataset come from NASA SRTM.

Figure 2: Morphostructural map of the Huallaga Basin from seismic interpretation and modified from Gil Rodriguez (2001), Hermoza et al. (2005) and Parsep Internal Report (2001). The location of the seismic lines is indicated by the red lines. Topographic dataset are from NASA SRTM.

Figure 3: Balanced cross section and sequential restorations across the Huallaga and Marañón Basins, from Calderon et al. (2017a).

Figure 4: Interpretation of line 91-mph-23 showing the structure of the Chazuta Thrust hangingwall and footwall in the central part of the basin. The Chazuta Thrust is a fault-bend-fold that accommodates a large horizontal displacement (at least 40 km). The footwall of this thrust is characterized by folded sedimentary series that seem to branch on a west-verging basement fault under the Chazuta Thrust front. The location of the line is indicated in Figure 2.

Figure 5: Interpretation of line 91-mph-24 (see location in Figure 2), illustrating the structure of the Chazuta Thrust hangingwall and footwall in the northern part of the basin. The Chazuta Thrust hangingwall is deformed by a backthrust and several small thrusts. High volumes of Permian evaporites (*décollement*) are incorporated in the hangingwall. The footwall is slightly folded and deformation is poorly imaged.

Figure 6: Interpretation of line 90-mph-02 (see location in Figure 2), illustrating the structure of the Chazuta Thrust hangingwall in the southern part of the basin. The Chazuta Thrust hangingwall is deformed by a pop-up structure. Again, the thick *décollement* is present in the Chazuta Thrust's hangingwall. To the West, the seismic profile images the eastern part of the fault-propagation fold Biabo Anticline. The structure of the Chazuta Thrust footwall is poorly imaged.

Figure 7: Experimental set up, modified from Santolaria et al. (2015). Deformation of the model was applied by a screw jack pulling the basal sheet. The morphostructural evolution of the model was monitored by two CCD cameras placed in an oblique and an azimuthal position.

Figure 8: Experimental protocol. A) Map-view illustrating the basal boundary conditions for all the models. The basal viscous *décollement* made of viscous polymer was a 65 cm long and 60 cm wide layer. B) and C) initial conditions of the models. The base of the models could be tilted. The thickness of the pre-kinematic tabular sand layers varied from 1.5 to 3 cm. Surface processes were tested by adding pre-kinematic or syn-kinematic wedges having varying thicknesses (Table 2), and by eroding the deformation front. D) Boundary conditions for each model.

913 Figure 9: Initial strength profiles of the experimental models.

914 Figure 10: A to E: Morphostructural sequence of the model Chaz_01. “S” stands for the
915 amount of shortening. F) Final cross section (the red dashed line indicates its position in
916 the final top view). The structures are numbered according to their chronological order of
917 their formation. “T” stands for the thrusts and “B” for the backthrusts. In map view, full
918 triangles indicate thrusts, and empty triangle backthrusts. The big grey arrows indicate the
919 direction towards which the basal film was pulled.

920 Figure 11: A to F) Morphostructural sequence of the model Chaz_02. G) Final cross section
921 (the red dashed line indicates its position on the final top view). On map views, the full
922 lines indicate the active structures, whereas dashed line indicate inactive thrusts. The rest
923 of the legend is the same as in Figure10.

924 Figure 12: A to F) Morphostructural sequence of the model Chaz_03. G). Final cross section
925 (the red dashed line indicates its position on the final top view). The legend is the same as
926 in Figure10.

927 Figure 13: A to F) Morphostructural sequence of the model Chaz_04. G) Final cross section
928 (the red dashed line indicates its position on the final top view). The legend is the same as
929 in Figure 10 and 11.

930 Figure 14: A to F) Morphostructural sequence of the model Chaz_05. G) Final cross section
931 (the red dashed line indicates its position on the final top view). The legend is the same as
932 in Figures 10 and 11.

933 Figure 15: A to F) Morphostructural sequence of the model Chaz_06. G) Final cross-section
934 (the red dashed line indicates its position on the final top view). The legend is the same as
935 in Figure 10.

936 Figure 16: A to F) Morphostructural sequence of the model Chaz_07. G) Final cross section
937 (the red dashed line indicates its position on the final top view). The legend is the same as
938 in Figure10.

939 **Table Caption**

940 Table 1: Scaling parameters and analogue material properties.

941 Table 2: Tested parameters. The first models tested the thickness of a flat sedimentary
942 overburden, then the impact of syn-kinematic sedimentation and of tilting the basal slope.
943 In models Chaz_06 and Chaz_07, we combined frontal erosion and pre-kinematic
944 deformation in addition to the previous parameters. “S” stands for the amount of
945 shortening.

946 Table 3: Initial stress values of the brittle overburden and the viscous décollement for each
947 experimental model.

948 **Supplementary material**

949 Supplementary material 1: Side-view movie of the Chaz_01 model.

950 Supplementary material 2: Side-view movie of the Chaz_02 model.

951 Supplementary material 3: Side-view movie of the Chaz_03 model.

952 Supplementary material 4: Side-view movie of the Chaz_04 model.

953 Supplementary material 5: Side-view movie of the Chaz_05 model.

954 Supplementary material 6: Side-view movie of the Chaz_06 model.

955 Supplementary material 7: Side-view movie of the Chaz_07 model.

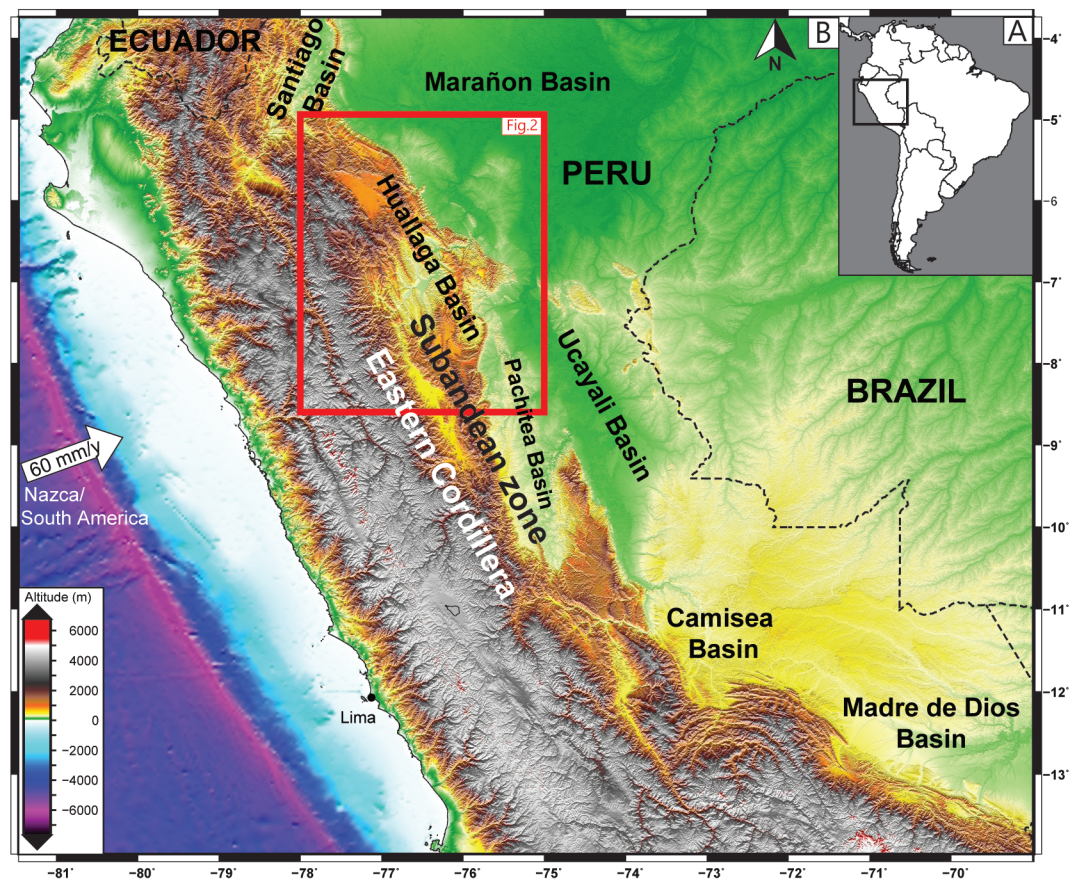

Figure 1: Topographic map of Peru illustrating the location of the Eastern Cordillera, the Subandean zone, and the main foreland basins of the Subandean zone. The study area (Huallaga Basin) is highlighted by the red square. Topographic dataset come from NASA SRTM.

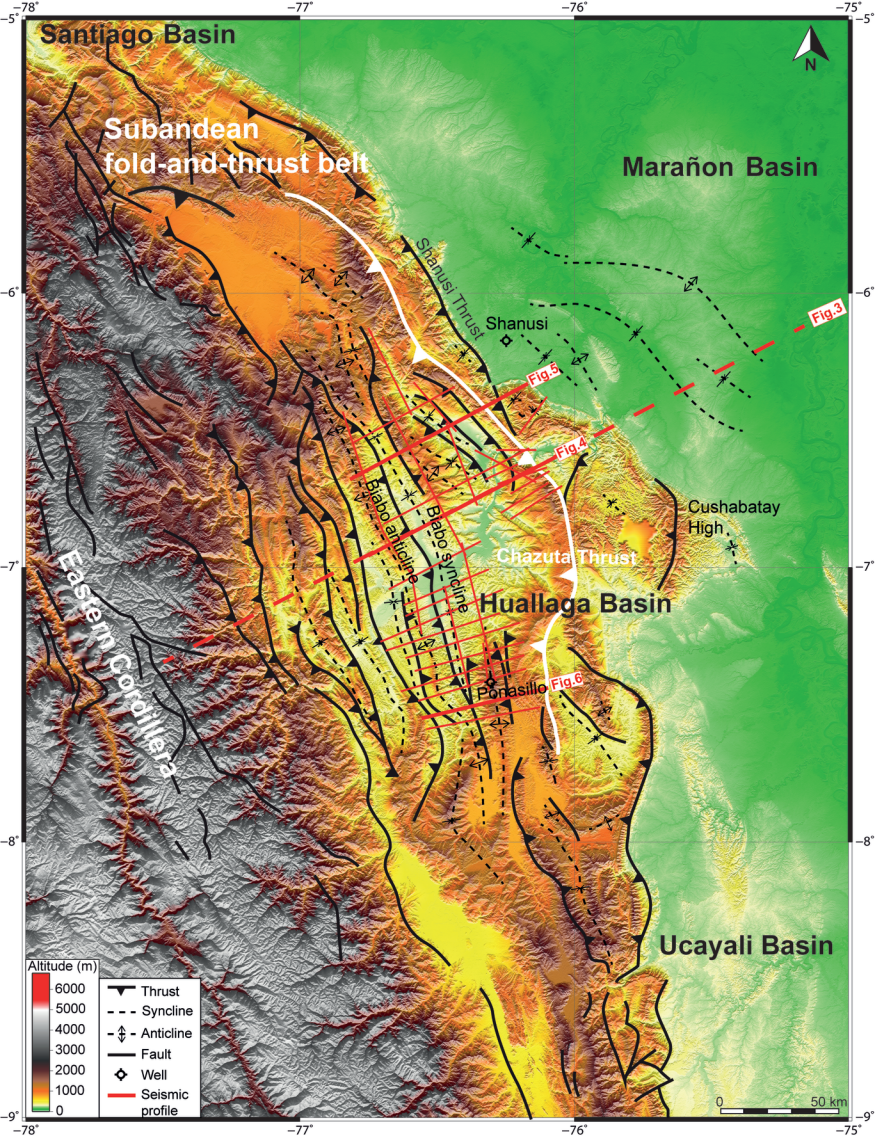

Figure 2: Morphostructural map of the Huallaga Basin, from seismic interpretation and modified from Gil Rodriguez (2001), Hermoza et al. (2005) and Parsep Internal Report (2001). The location of the seismic lines is indicated by the red lines. Topographic dataset are from NASA SRTM.

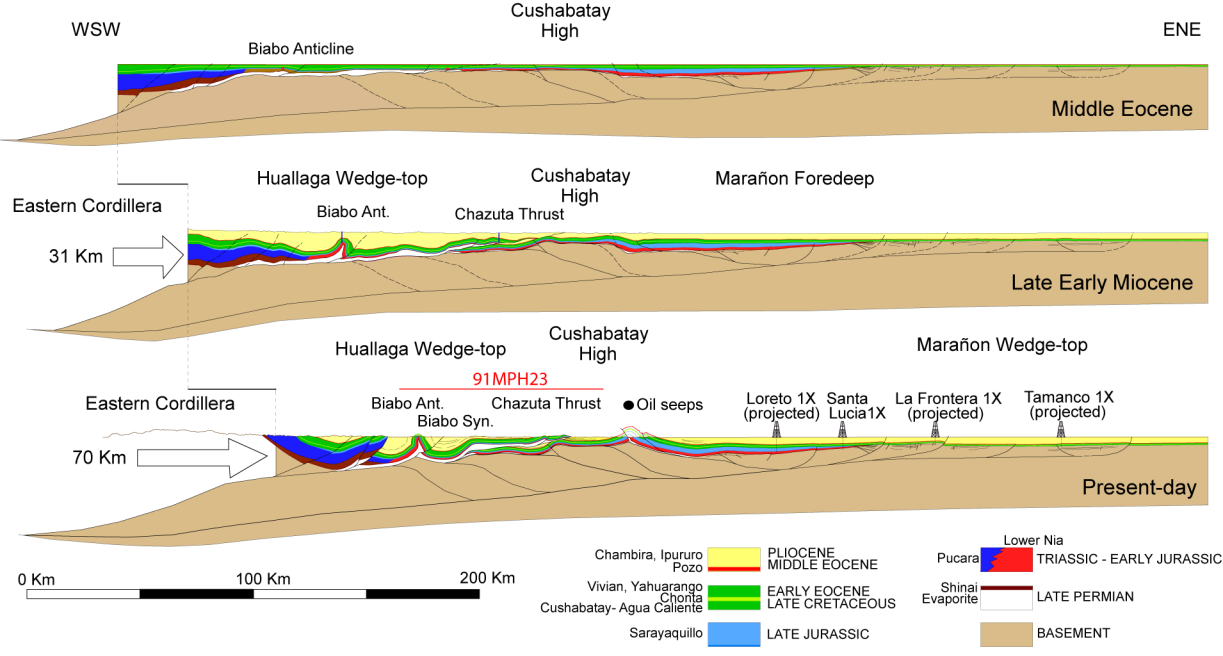

Figure 3: Balanced cross section and sequential restorations across the Huallaga and Marañón Basins, from Calderon et al. (2017a).

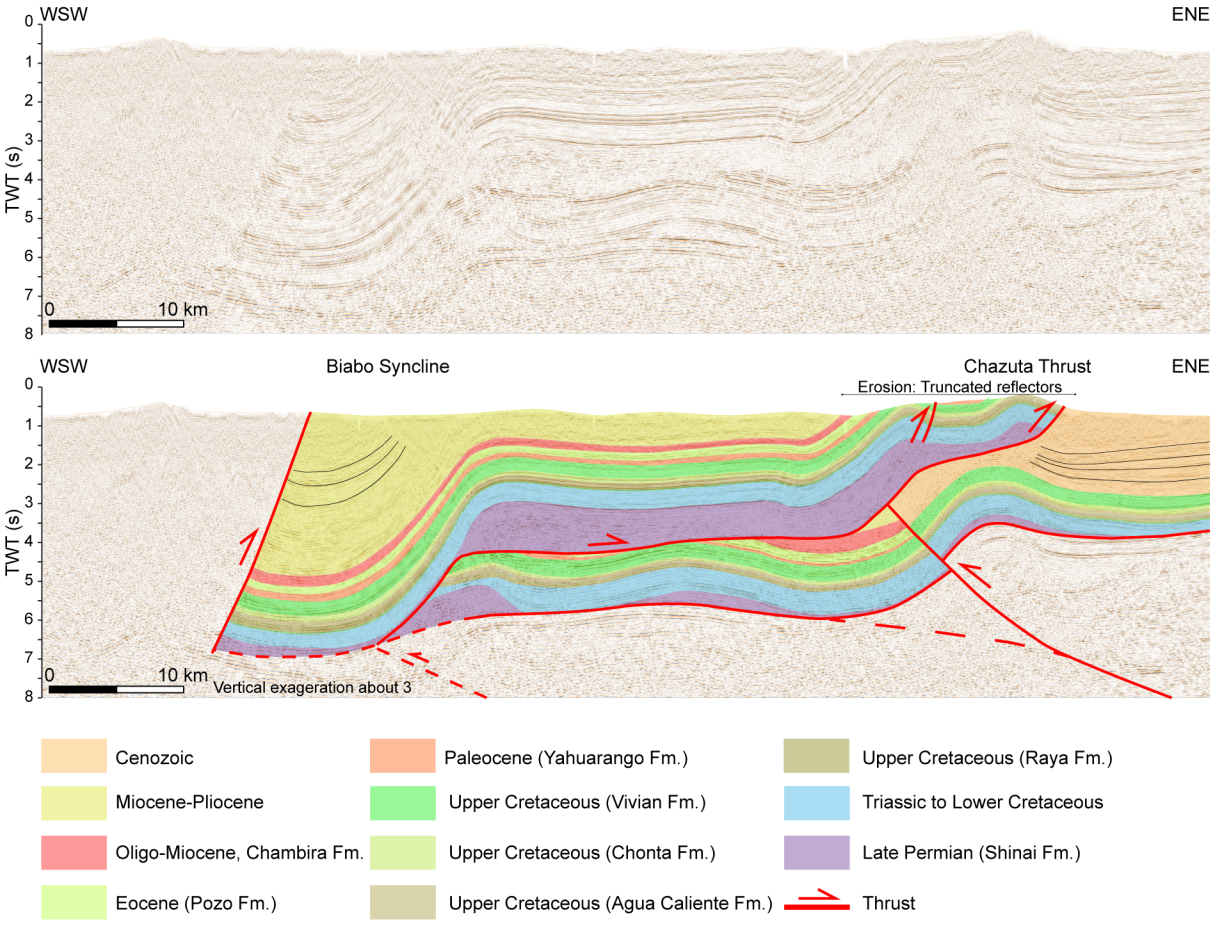

Figure 4: Interpretation of line 91-mph-23 showing the structure of the Chazuta Thrust hangingwall and footwall in the central part of the basin. The Chazuta Thrust is a fault-bend-fold that accommodates a large horizontal displacement (at least 40 km). The footwall of this thrust is characterized by folded sedimentary series that seem to branch on a west-verging basement fault under the Chazuta Thrust front. The location of the line is indicated in the Figure 2.

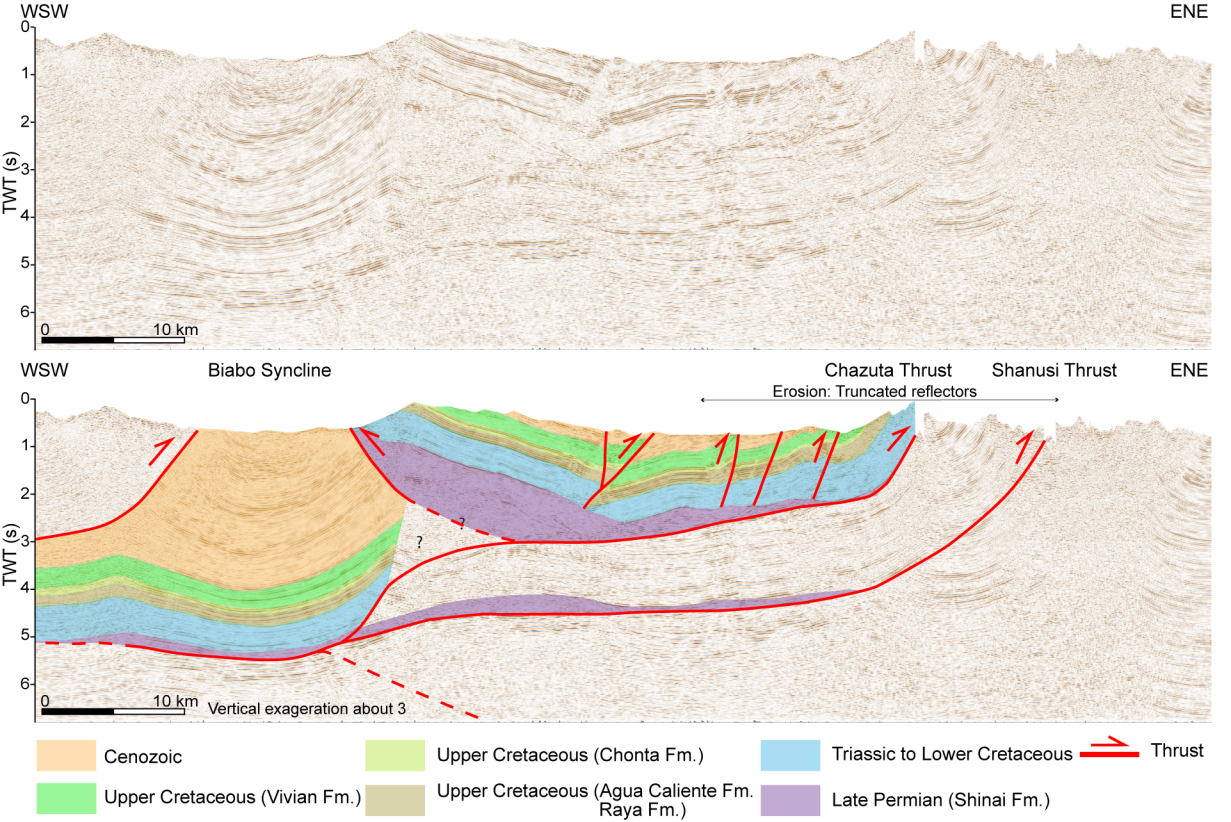

Figure 5: Interpretation of line 91-mph-24 (see location in Figure 2), illustrating the structure of the Chazuta Thrust hangingwall and footwall in the northern part of the basin. The Chazuta Thrust hangingwall is deformed by a backthrust and several small thrusts. High volumes of Permian evaporites (décollement) are incorporated in the hangingwall. The footwall is slightly folded and deformation is poorly imaged.

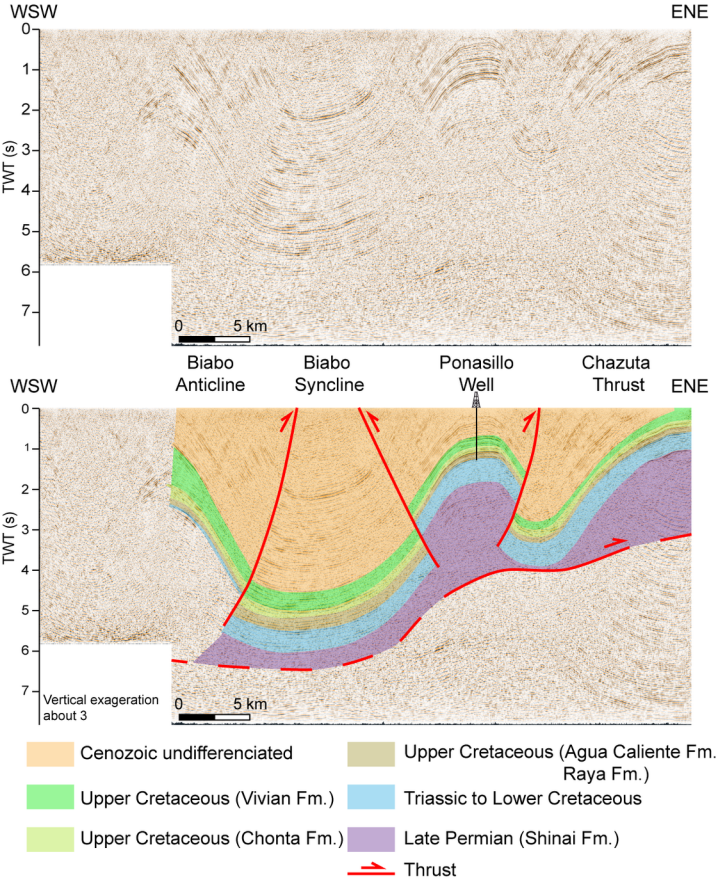

Figure 6: Interpretation of line 90-mph-02 (see location in Figure 2), illustrating the structure of the Chazuta Thrust hangingwall in the southern part of the basin. The Chazuta Thrust hangingwall is deformed by a pop-up structure. Again, the thick décollement is present in the Chazuta's Thrust hangingwall. To the West, the seismic images the eastern part of the fault-propagation fold Biabo Anticline. The structure of the Chazuta Thrust footwall is poorly imaged.

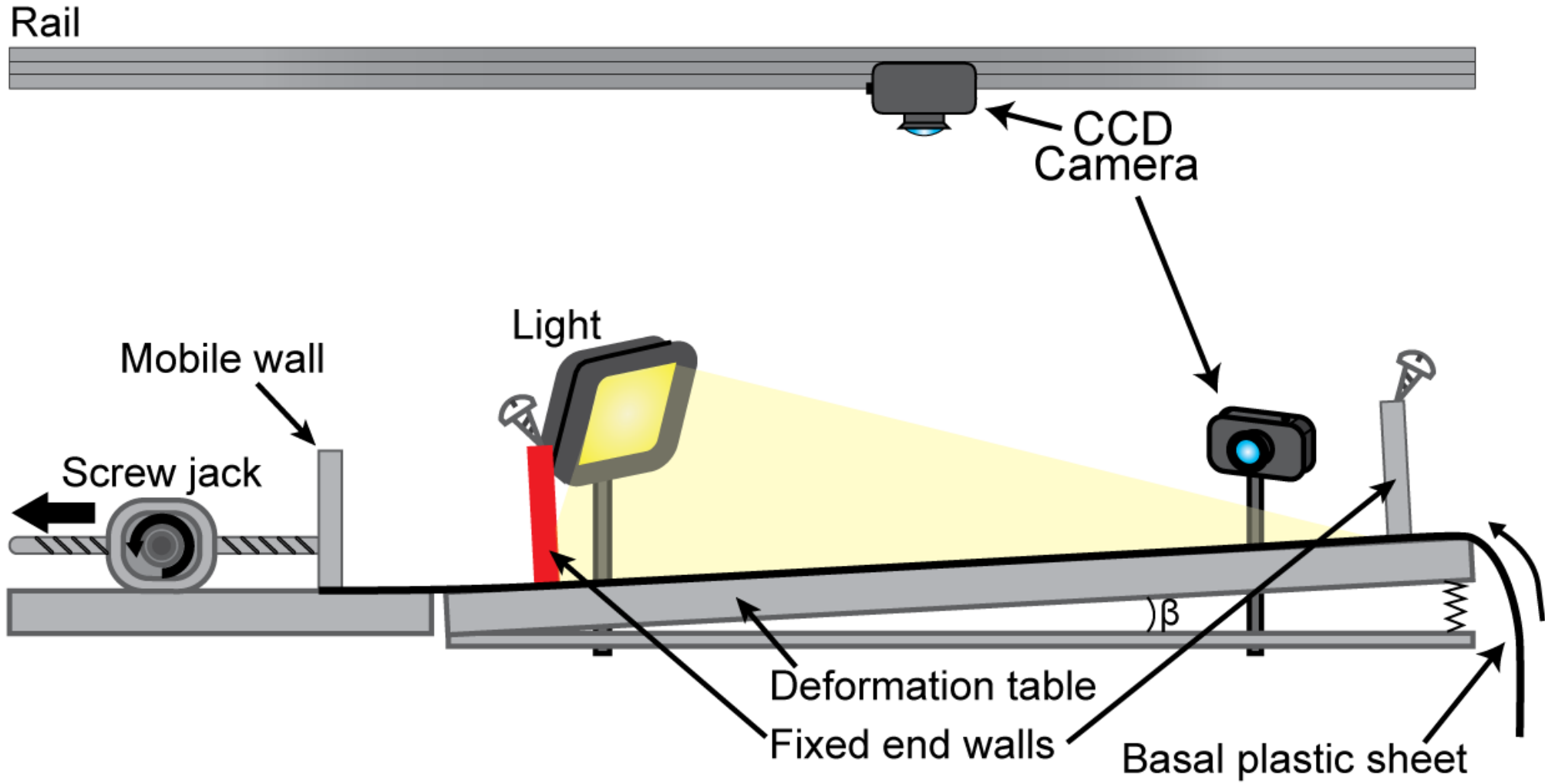

Figure 7: Experimental set-up modified from Santolaria et al. (2015). Deformation of the model was applied by a screw-jack pulling the basal sheet. The morphostructural evolution of the model was monitored by two CCD cameras placed in an oblique and in an azimuthal position.

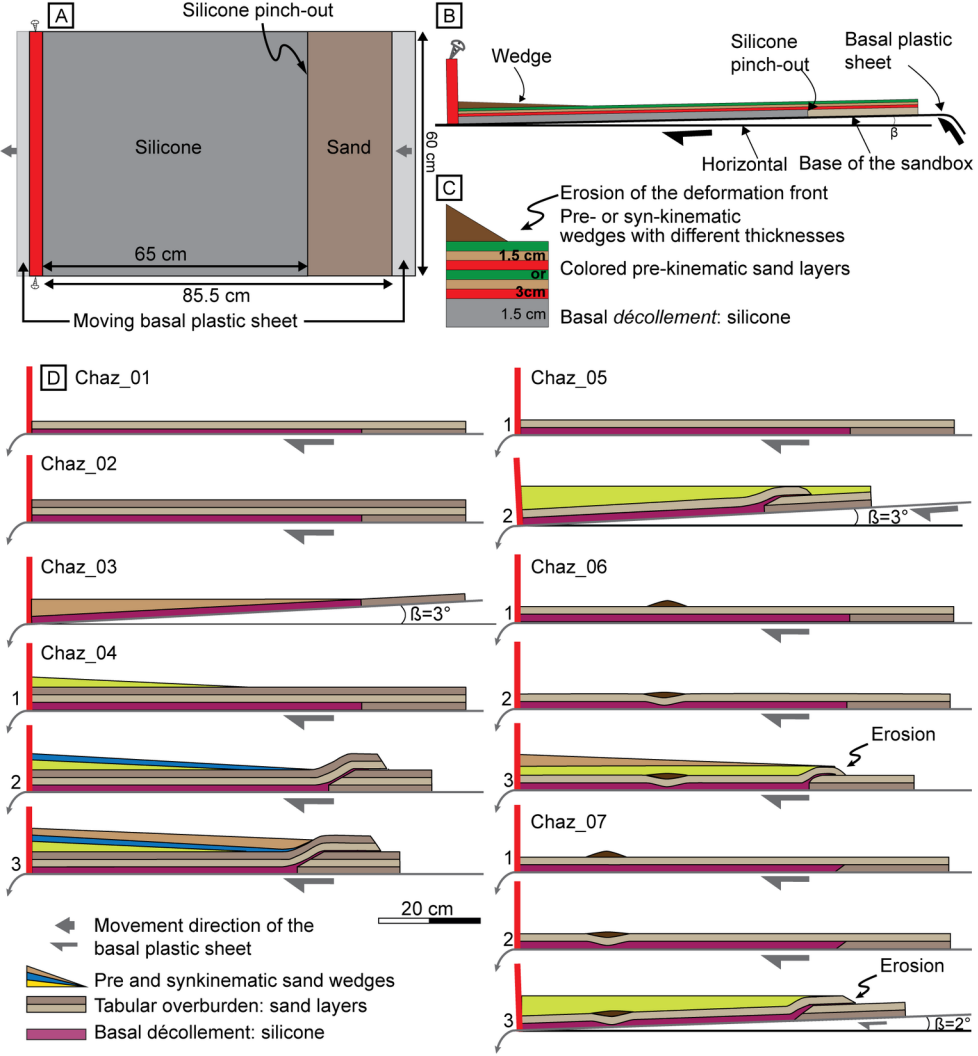

Figure 8: Experimental protocol. A) Map-view illustrating the basal boundary conditions for all the models. The basal viscous décollement was a 65 cm long and 60 cm wide layer of viscous polymer. B) and C) initial conditions of the models. The base of the models could be tilted. The thickness of the pre-kinematic tabular sand layers varied from 1.5 to 3 cm. Surface processes were tested by adding pre-kinematic or syn-kinematic wedges having different thicknesses (Table 1), and by eroding the deformation front. D) Boundary conditions of each model.

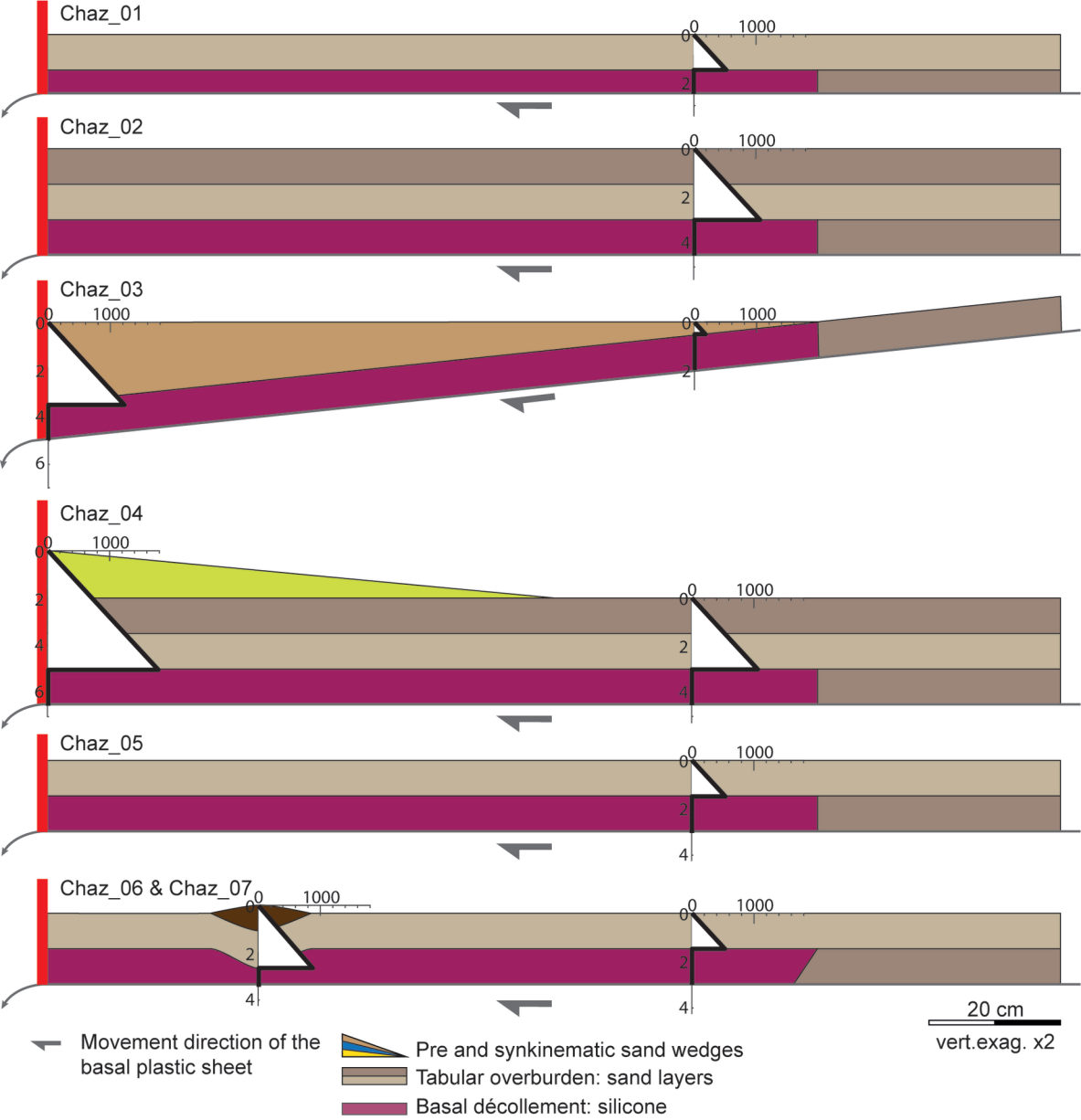

Figure 9: Initial strength profiles of the experimental models.

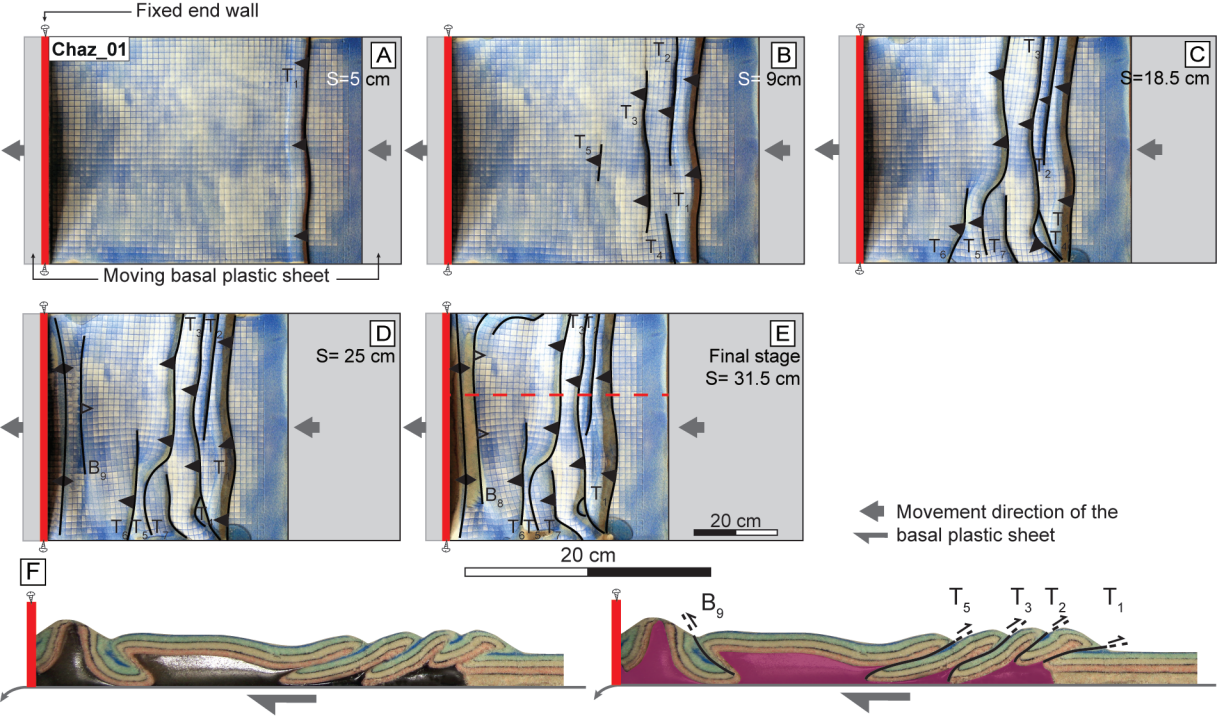

Figure 10: A to E: Morphostructural sequence of the Chaz_01 model. "S" stands for the amount of shortening. F) Final cross section (the red dashed line indicates its position in the final top view). The structures are numbered according to their chronological order of their formation. "T" stands for the thrusts and "B" for the backthrusts. In map view, full triangles indicate thrusts, and empty triangle backthrusts. The big grey arrows indicate the direction towards which the basal film was pulled.

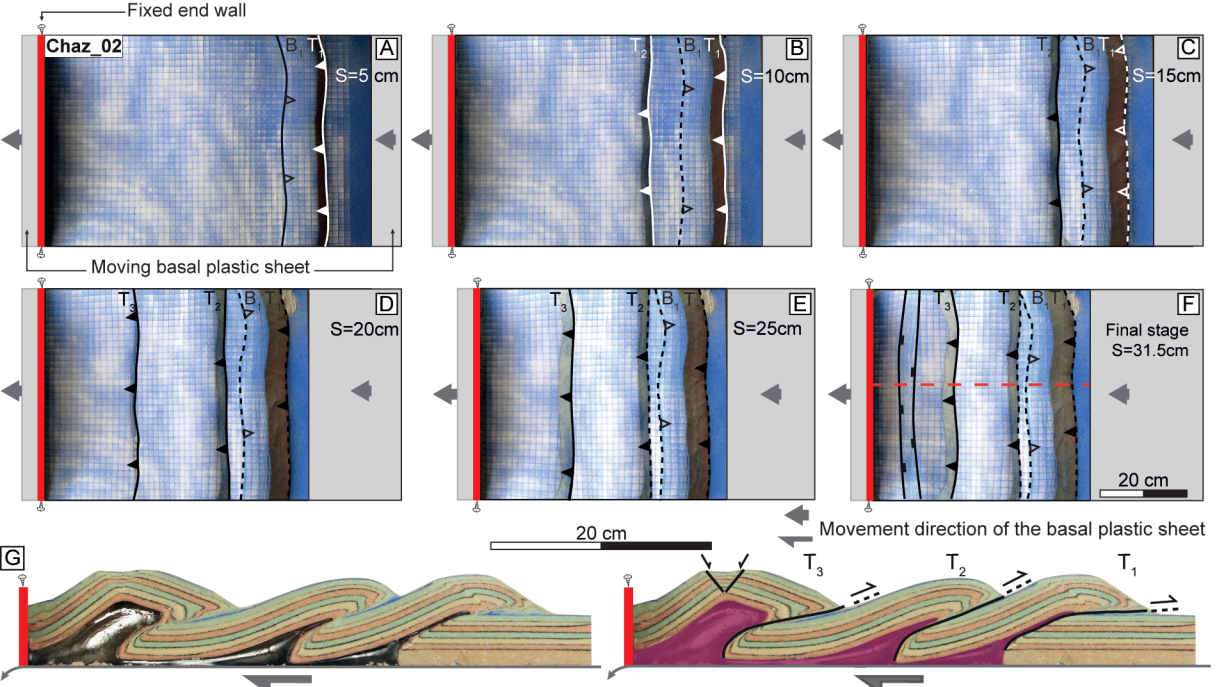

Figure 11: A to F) Morphostructural sequence of the Chaz_02 model. G) Final cross section (the red dashed line indicates its position on the final top view). On map views, the full lines indicate the active structures, whereas dashed line indicate inactive thrusts. The rest of the legend is the same as in Figure 9.

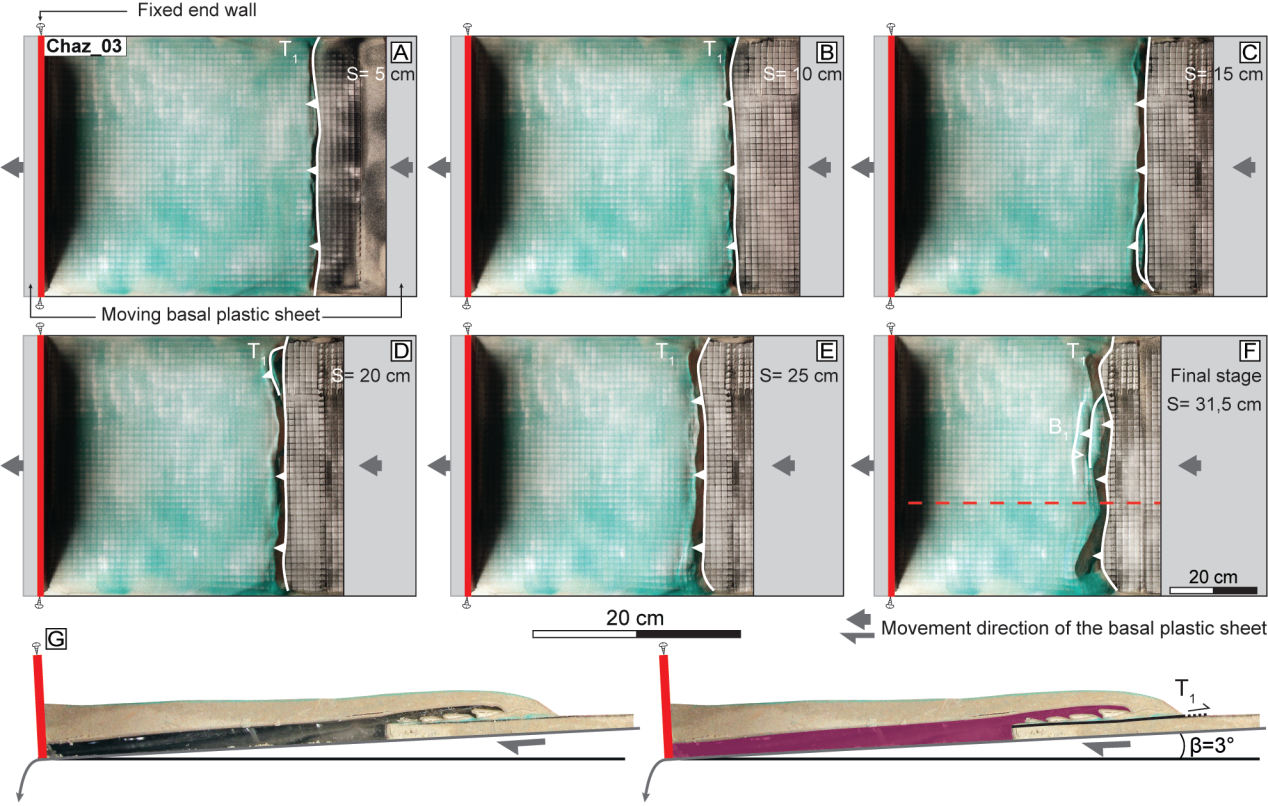

Figure 12: A to F) Morphostructural sequence of the Chaz_03 model. G) Final cross section (the red dashed line indicates its position on the final top view). The legend is the same as Figure 9.

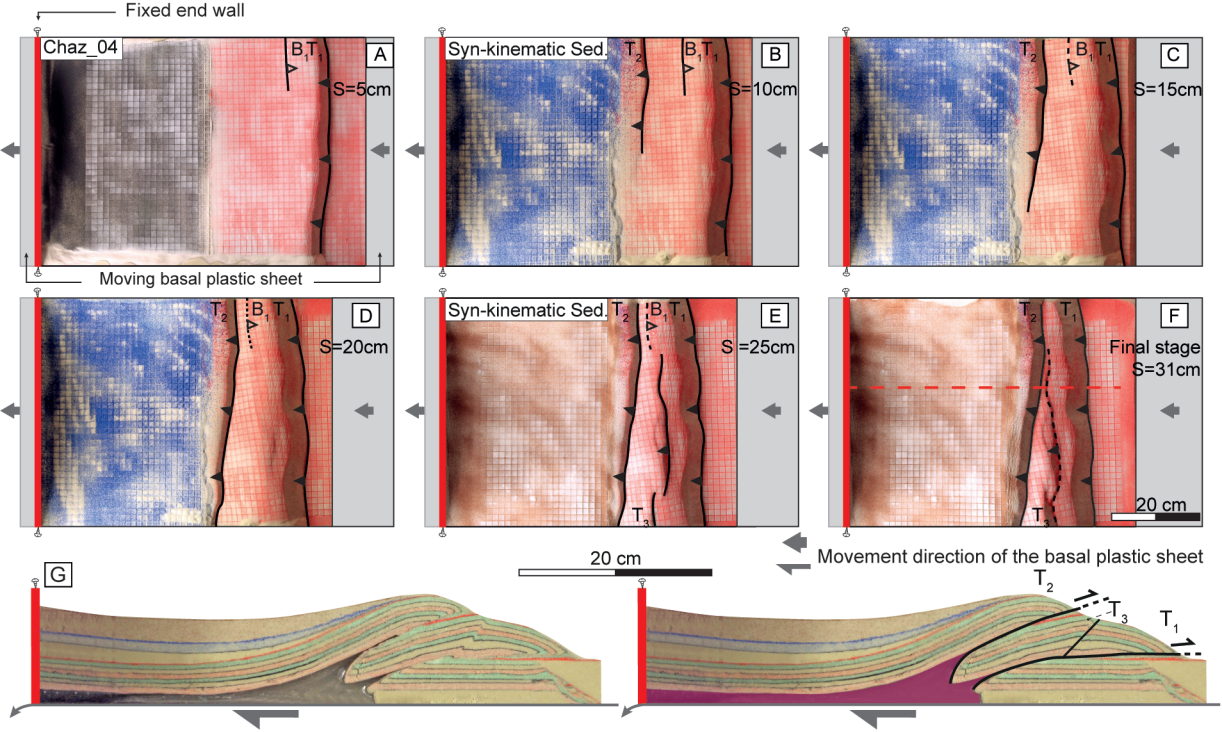

Figure 13: A to F) Morphostructural sequence of the Chaz_04 model. G) Final cross section (the red dashed line indicates its position on the final top view). The legend is the same as Figures 9 and 10.

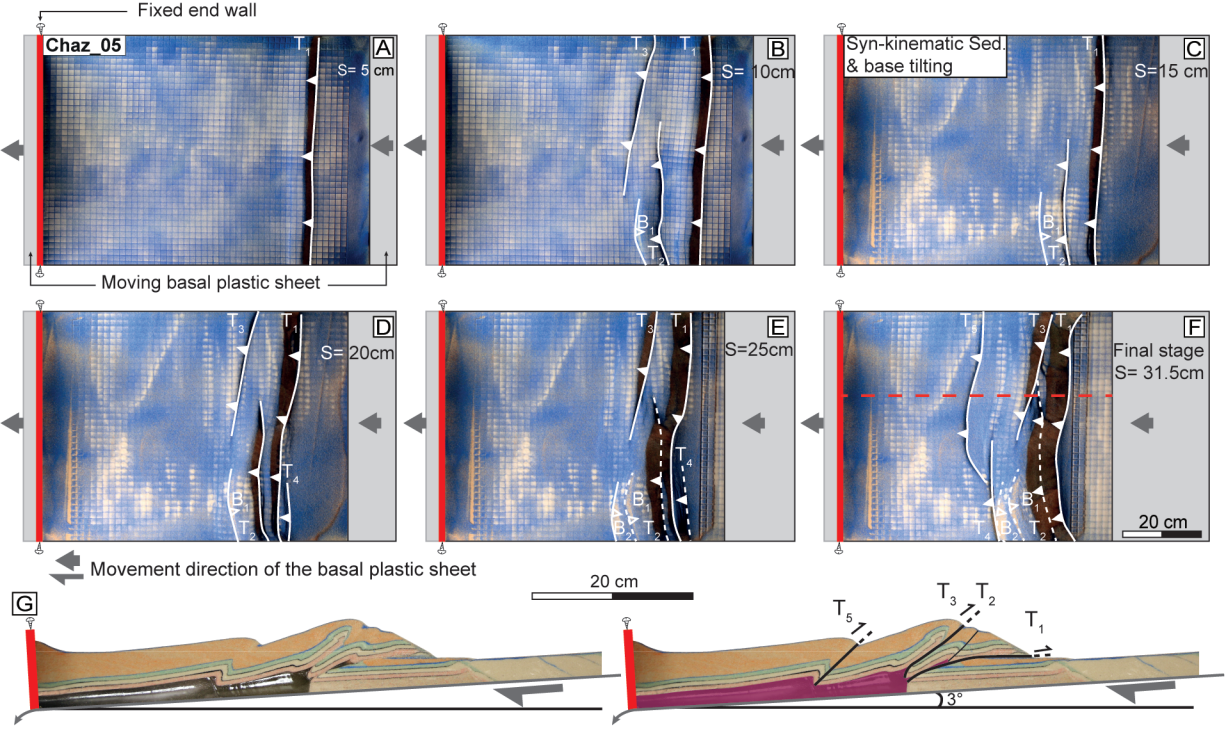

Figure 14: A to F) Morphostructural sequence of the Chaz_05 model. G) Final cross section (the red dashed line indicates its position on the final top view). The legend is the same as in Figures 9 and 10.

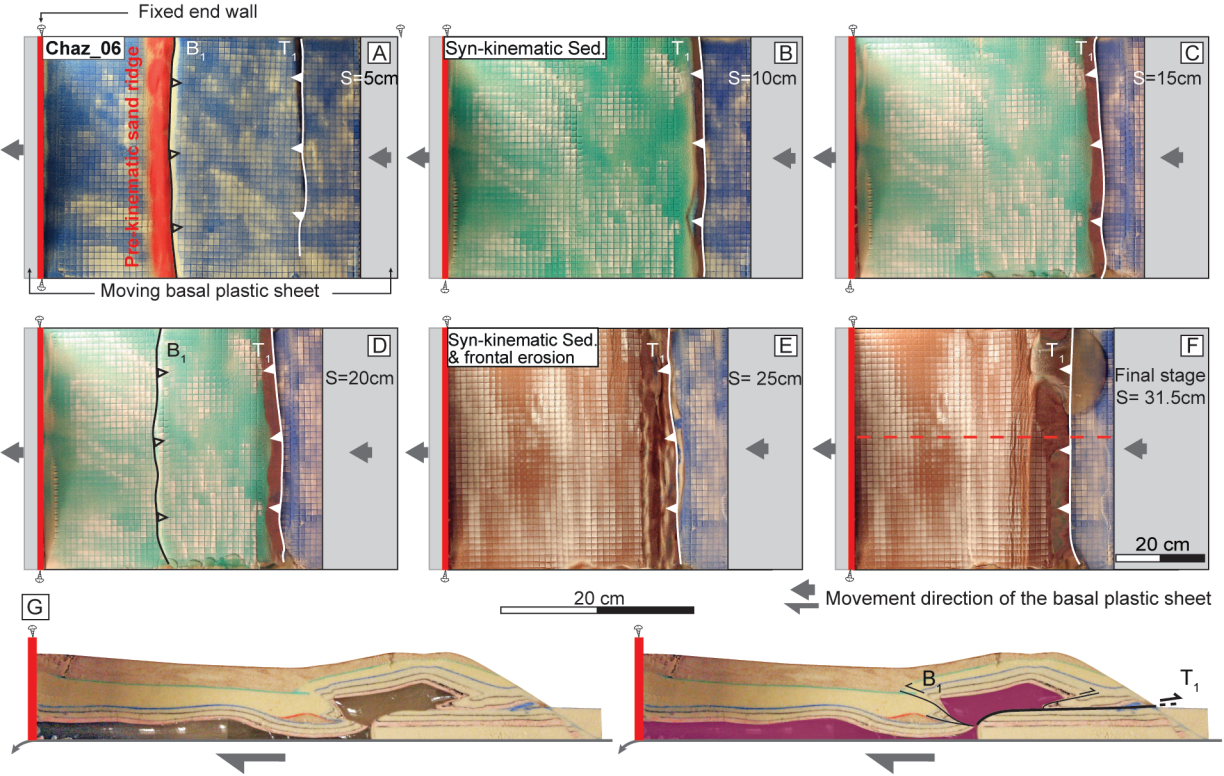

Figure 15: A to F) Morphostructural sequence of the Chaz_06 model. G) Final cross-section (the red dashed line indicates its position on the final top view). The legend is the same as in Figure 9.

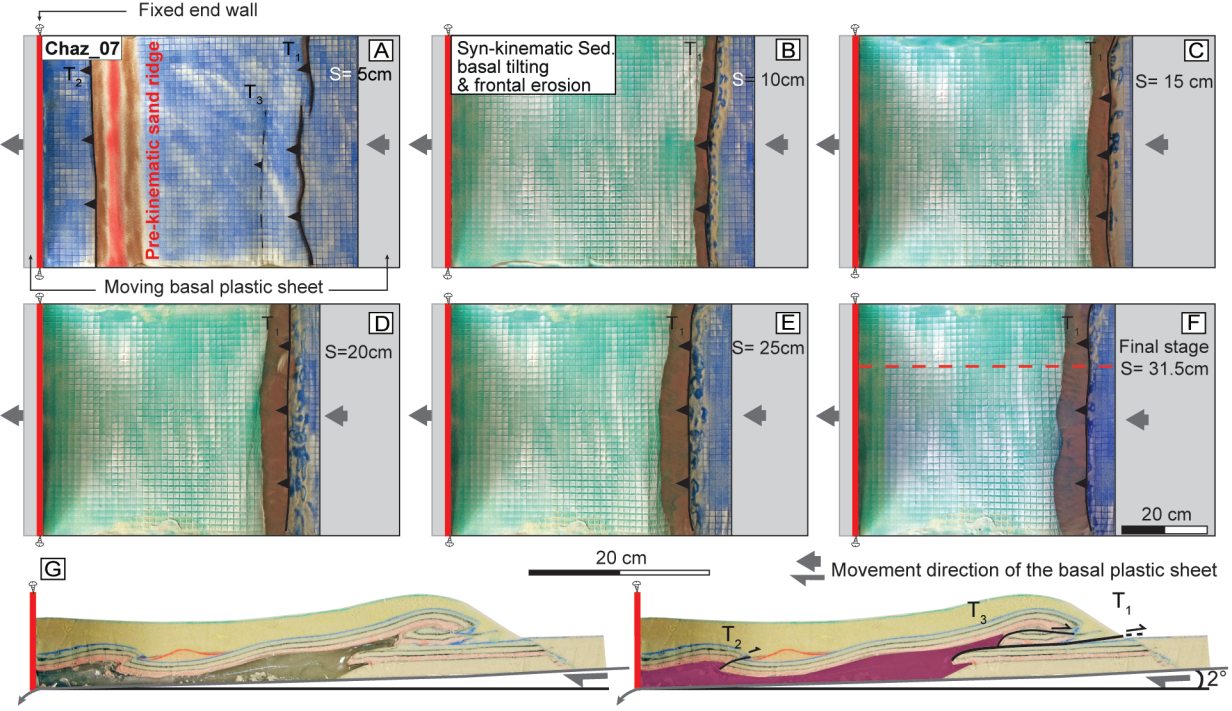

Figure 16: A to F) Morphostructural sequence of the Chaz_07 model. G) Final cross section (the red dashed line indicates its position on the final top view). The legend is the same as in Figure 9.

Parameter	Model	Nature	Model to Nature ratio
Length, L (m)	0.01	1500	0.66×10^{-5}
Gravity, g ($m.s^{-2}$)	9.81	9.81	1
Brittle overburden GA39 dry sand			
Density, ρ ($g.cm^{-3}$)	1.4	2.6	0.54
Cohesion, c (Pa)	≈ 40	$10\text{-}30 \times 10^{6}$	$\approx 1.3 \times 10^{-6}$
Internal friction coefficient, μ	≈ 0.7	0.6-0.85	
Brittle overburden NE34 dry sand			
Density, ρ ($g.cm^{-3}$)	1.6	2.6	0.62
Cohesion, c (Pa)	≈ 60	$10\text{-}30 \times 10^{6}$	$\approx 2 \times 10^{-6}$
Internal friction coefficient, μ	≈ 0.6	0.6-0.85	
Viscous *décollement*			
Density, ρ (g.cm-3)	0.965	2.2	0.44
Viscosity, η (Pa.s)	2.2×10^{4}	5×10^{18}	4.4×10^{-15}
Stress, σ=ρ x g x L (Pa)			3.33×10^{-6}
Strain rate, Ɛ=σ/η (s^{-1})			7.5×10^{8}
Time, t=1/Ɛ (s)	3600	2.7×10^{12} (85000 y)	1.33×10^{-9}
	65 h	5.6 My	
Shortening rate, v = Ɛ x L	5 mm/h	9 mm/yr	4950

Table 1: Scaling parameters and analogue material properties.

Model #	**Chaz_01**	**Chaz_02**	**Chaz_03**	**Chaz_04**	**Chaz_05**	**Chaz_06**	**Chaz_07**
Sidewalls lubrication	Yes	Yes	None	Yes	None	Yes	Yes
Décollement thickness (cm)	1	1.5	1.5	1.5	1.5	1.5	1.5
Tabular overburden thickness (cm)	1.5	3	0	3	1.5	1.5	1.5
Prekinematic wedge maximum thickness (cm)	None	None	3.5	2	None	None	None
Synkinematic wedge - number and maximum thickness (cm)	None	None	None	1 - 1.2 2 - 3	1 - 4	1 - 4 2 - 3	1 - 3.3
Décollement dip (β)	0	0	3° prekinematic	0	3° at S = 10 cm	0	2° at S= 7.5 cm
Prekinematic deformation: early syncline	None	None	None	None	None	at 28 cm from the western backstop	at 18 cm from the western backstop
Frontal erosion	None	None	None	None	None	at S=21cm	During the whole shortening

Table 2: Tested parameters. The first models tested the thickness of a flat sedimentary overburden, then the impact of syn-kinematic sedimentation and of tilting the basal slope. In models Chaz_06 and Chaz_07, we combined frontal erosion and pre-kinematic deformation in addition to the previous parameters. “S” stands for the amount of shortening.

Model #	σ_v (=σ_3) (Pa)	σ_1 (Pa)	σ_1-σ_3 (Pa)	τ_d (Pa)	R=σ_1-σ_3/τ_d
Chaz_01	221	749	529	3	173
Chaz_02	441	1499	1057	2	519
Chaz_03 max (backstop)	515	1749	1234	2	606
Chaz_03 min (wedge toe)	74	250	176	2	87
Chaz_04 max (backstop)	736	2498	1762	2	865
Chaz_04 min (wedge toe)	441	1499	1057	2	519
Chaz_05	221	749	529	2	260
Chaz_06 max (flat overburden + subsided ridge)	368	1249	881	4	216
Chaz_06 min (flat overburden)	221	749	529	2	260
Chaz_07 max (flat overburden + subsided ridge)	368	1249	881	4	216
Chaz_07 min (flat overburden)	221	749	529	2	260

Table 3: Initial stress values of the brittle overburden and the viscous *décollement* for each experimental model.